



HAL
open science

The milankovitch fingerprint on the distribution and thickness of bedding-parallel veins (beef) in source rocks

E. Ravier, Mathieu Martinez, Pierre Pellenard, Alain Zanella, Lucie Tupinier

► To cite this version:

E. Ravier, Mathieu Martinez, Pierre Pellenard, Alain Zanella, Lucie Tupinier. The milankovitch fingerprint on the distribution and thickness of bedding-parallel veins (beef) in source rocks. *Marine and Petroleum Geology*, 2020, 122, pp.104643. 10.1016/j.marpetgeo.2020.104643 . insu-02922274

HAL Id: insu-02922274

<https://insu.hal.science/insu-02922274v1>

Submitted on 26 Aug 2020

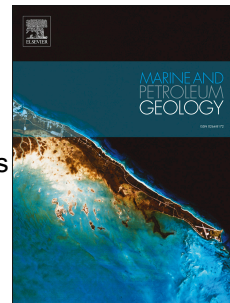
HAL is a multi-disciplinary open access archive for the deposit and dissemination of scientific research documents, whether they are published or not. The documents may come from teaching and research institutions in France or abroad, or from public or private research centers.

L'archive ouverte pluridisciplinaire **HAL**, est destinée au dépôt et à la diffusion de documents scientifiques de niveau recherche, publiés ou non, émanant des établissements d'enseignement et de recherche français ou étrangers, des laboratoires publics ou privés.

Journal Pre-proof

The milankovitch fingerprint on the distribution and thickness of bedding-parallel veins (beef) in source rocks

Edouard Ravier, Mathieu Martinez, Pierre Pellenard, Alain Zanella, Lucie Tupinier



PII: S0264-8172(20)30426-8

DOI: <https://doi.org/10.1016/j.marpetgeo.2020.104643>

Reference: JMPG 104643

To appear in: *Marine and Petroleum Geology*

Received Date: 16 April 2020

Revised Date: 3 July 2020

Accepted Date: 3 August 2020

Please cite this article as: Ravier, E., Martinez, M., Pellenard, P., Zanella, A., Tupinier, L., The milankovitch fingerprint on the distribution and thickness of bedding-parallel veins (beef) in source rocks, *Marine and Petroleum Geology* (2020), doi: <https://doi.org/10.1016/j.marpetgeo.2020.104643>.

This is a PDF file of an article that has undergone enhancements after acceptance, such as the addition of a cover page and metadata, and formatting for readability, but it is not yet the definitive version of record. This version will undergo additional copyediting, typesetting and review before it is published in its final form, but we are providing this version to give early visibility of the article. Please note that, during the production process, errors may be discovered which could affect the content, and all legal disclaimers that apply to the journal pertain.

© 2020 Published by Elsevier Ltd.

Credit author statement

Edouard Ravier: conceptualization, investigation, visualization, writing original draft

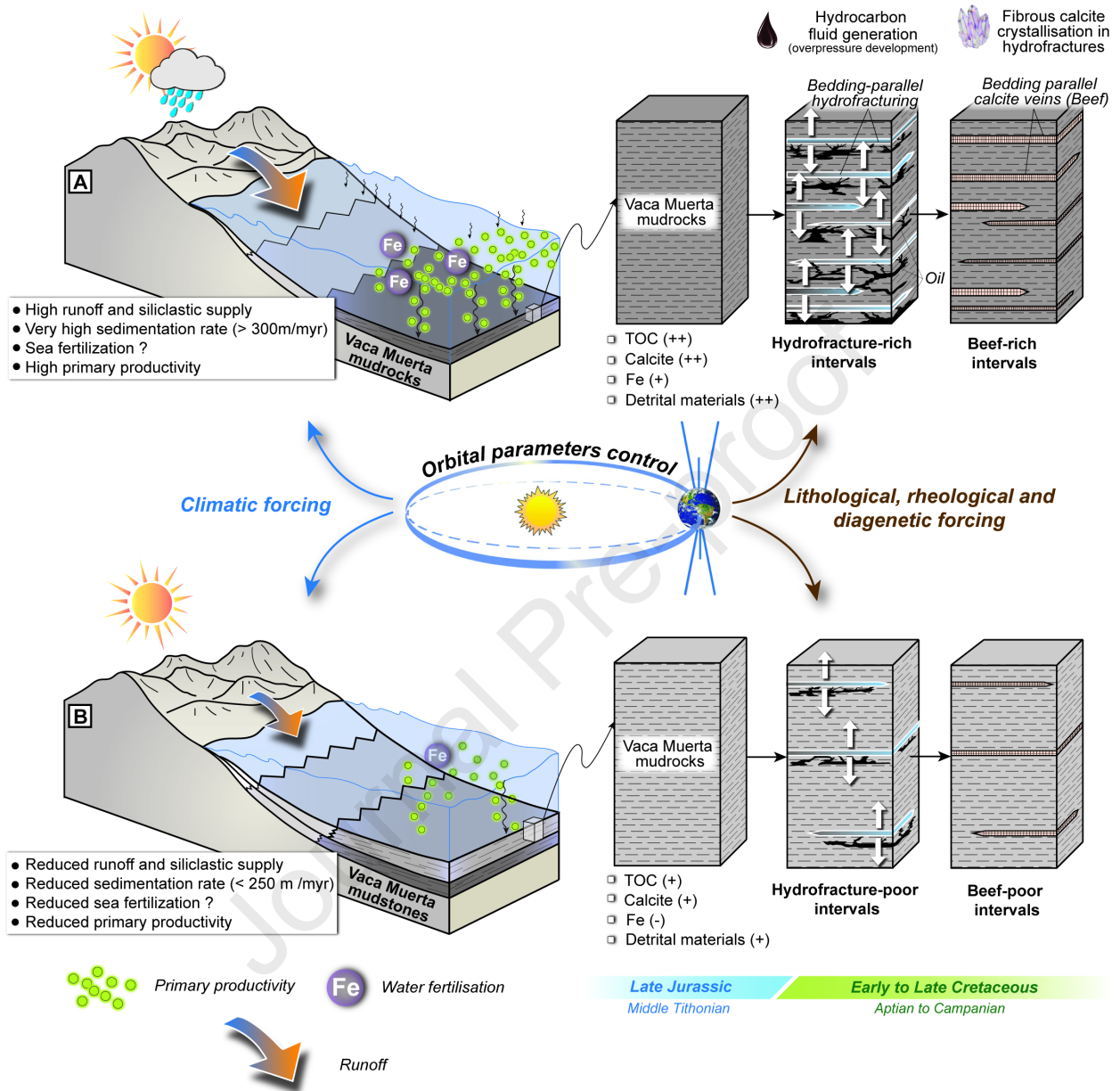
Mathieu Martinez: conceptualization, methodology, investigation, formal analysis, writing original draft

Pierre Pellenard : conceptualization, methodology, review and editing

Alain Zanella : conceptualization, investigation, review and editing

Lucie Tupinier : investigation, formal analysis

Journal Pre-proof



1 **The Milankovitch fingerprint on the distribution and thickness of bedding-parallel veins**
2 **(beef) in source rocks**

3

4 Edouard Ravier^a, Mathieu Martinez^b, Pierre Pellenard^c, Alain Zanella^a, Lucie Tupinier^c

5

6 *a. Le Mans Université, Géosciences Le Mans - LPG UMR 6112, 72085 Le Mans, France*

7 *b. Univ Rennes, CNRS, Géosciences Rennes - UMR 6118, F-35000 Rennes, France*

8 *c. Biogéosciences, UMR CNRS/uB 6282, Université Bourgogne Franche-Comté, F-21000 Dijon, France*

9

10 **Abstract**

11

12 Bed-parallel, mineralized fractures are common in source rocks and generally consist in mm
13 to cm thick veins developed parallel to bedding known as beef or bedding-parallel veins.

14 Considering they can form a dense network of mechanical discontinuities, the prediction of
15 beef distribution is a major issue impacting shale reservoir production. Beef distribution is

16 predominantly controlled by the lithological characteristics of source rocks and we here
17 decipher the relation between mineralogical and chemical proxies controlled by orbital

18 parameters and distribution of the beef along a Late Jurassic section of the well-known Vaca
19 Muerta Formation source rock in the Neuquén Basin. Using multiple proxies collected along

20 the beef-rich Huncal section, we show that Milankovitch cycles rule the mineralogical
21 evolution and beef distribution in these organic-rich mudrocks. Cycles inferred from the

22 statistical treatment of sedimentary (magnetic susceptibility, elemental and mineralogical
23 ratios), biogenic (total organic carbon) and diagenetic (beef distribution and thickness) signals

24 revealed indeed the influence of an astroclimatic fingerprint in sediments and on processes
25 controlling mineralized fracture generation and distribution. The astroclimatic memory

26 recorded in many source rocks worldwide is therefore envisaged as a suitable proxy for the
27 prediction of mineralized fracture distribution.

28

29 **Keywords:** beef; bedding-parallel veins; Milankovitch cycles; astroclimatic forcing;
30 diagenesis; source rocks.

31

32 Corresponding author: Edouard Ravier; Edouard.ravier@univ-lemans.fr

33

34 **1. Introduction**

35

36 During burial and diagenesis, sediments can reach a state of overpressure at depth when the
37 pore fluid pressure becomes greater than that of an equivalent free column of water
38 (hydrostatic pressure). The burial of organic-rich mudrock (e.g., source rock) is commonly
39 associated with the development of fluid overpressures due to mechanical and chemical
40 compaction of clay and thermal maturation of kerogen (Grauls, 1997; Swarbrick et al., 2002;
41 Cobbold and Rodrigues, 2007). The release of water and genesis of oil and gas within low-
42 permeability source rocks is responsible for a drastic increase of their pore-fluid pressure. In
43 response to this distributed overpressure, hydrofractures can develop parallel to bedding
44 (Cosgrove, 1995; Rodrigues et al., 2009; Gale et al., 2014; Zhang et al., 2016). The
45 occurrence of bedding parallel fibrous veins in source rocks has commonly been interpreted
46 as the mineralisation of such hydrofractures (Cobbold et al., 2013). These veins, also referred
47 to as beef or Bedding-Parallel Veins (BPV), are mostly composed of fibrous calcite although
48 gypsum or quartz veins have been described in the literature (Cobbold et al., 2013 and
49 references therein). Inclusions of either liquid (oil) or solid (bitumen) hydrocarbons in the
50 veins illustrate the relative synchronicity between kerogene cracking, hydrofracturing and

51 precipitation of supersaturated aqueous solutions (Rodrigues et al., 2009; Zanella et al.,
52 2015b). The occurrence of BPV in organic-rich sediment of low maturity has also led to
53 suggest that beef may be produced during sediment degassing and/or rapid deposition of the
54 overlying sediments or by the combination of pressure solution and the driving force of
55 crystallization (Meng et al., 2017, 2018). The common occurrence of BPVs in foreland basins
56 worldwide suggests that their formation is often a consequence of both fluid overpressures
57 and compressional tectonic stress (Zanella et al., 2020).

58 Some organic-rich sediments display intervals with very high beef concentration. The
59 Jurassic-Cretaceous black shales of the Vaca Muerta Formation (Argentina) or the Charmouth
60 Mudstone Formation with the so-called “Shales-with-beef Member” (England) are among the
61 best examples of section gathering tens of closely-spaced horizontal and fibrous calcite veins
62 (Rodrigues et al., 2009; Zanella et al., 2015a,b; Meng et al., 2017). Beef can reach up to 10%
63 of the rock volume for some intervals of the Vaca Muerta Fm in the Huncal area, with
64 thickness ranging from a few millimeters to 16 centimeters for individual BPVs (Rodrigues et
65 al., 2009). Weger et al (2019) provided a high-resolution logging of beef distribution in a 800
66 meters thick section of Vaca Muerta Formation (Puerta Curaco area) and showed that more
67 than 50 meters of the section contains an excess of 2% beef measured by percentage of rock
68 volumes. Similarly, Lejay et al (2017) estimated a proportion of 2 to 3% of beef throughout
69 the Vaca Muerta Fm using core data from the eastern part of the Neuquén basin.

70 Knowing that mineralized fractures behave as major mechanical discontinuities in source
71 rocks and influence both hydraulic fracture stimulation and production (Gale et al., 2014), the
72 prediction of beef distribution is therefore a major issue as many studies aim to better
73 constrain the mechanical properties of source rocks. The location, distribution and thickness
74 of BPV are thought to be organized and controlled by several parameters related to the total
75 organic carbon in sediments, the maturation of organic matter, the nature and content of

76 carbonate and any types of rheological heterogeneities in the host rock that could alter its
77 geomechanics and provide space or a nucleus for carbonate precipitation (Gale et al., 2014;
78 Lejay et al., 2017; Meng et al., 2017, 2018). These parameters are mainly inherited from
79 palaeoenvironmental conditions during mudstone deposition because the grain-size,
80 mineralogy and organic content of sediments are most often related to the combination of
81 climatic and eustatic variations, especially for organic-rich sediments from a marine origin.
82 Some correlations (sometimes very weak) between beef distribution and ash beds or
83 diagenetic concretions described in some parts of the Neuquén Basin implies that rheological
84 heterogeneities and mechanical contrast in mudstone can also be related to the local imprint of
85 aerial explosive volcanism or to the superimposed diagenetic signature for examples (Lejay et
86 al., 2017; Weger et al, 2019).

87 The Earth experiences periodic changes in the eccentricity, inclination and orientation of the
88 Ecliptic plane as well as periodic motions of its rotational axis (see also Hinnov, 2018 for a
89 review). The orbital parameters resulting from these motions are: (i) the eccentricity, which is
90 the change of the shape of the Ecliptic plane from the perfect circle to an ellipse. The
91 eccentricity cycles have main periods of ~100 kyr, 405 kyr and 2.4 Myr (Laskar et al., 2011);
92 (ii) the obliquity, which is the angle between the perpendicular to the Ecliptic plane and the
93 Earth's rotational axis. The obliquity cycles have a main period calculated at 38.0 ± 1.7 kyr in
94 the Tithonian (Waltham, 2015) and (iii) the climatic precession, which corresponds to the drift
95 of the Earth-Sun distance at a given date of the year. The climatic precession cycles have an
96 average period calculated at 20.2 ± 0.5 kyr in the Tithonian (Waltham, 2015). These orbital
97 parameters modify cyclically the difference in insolation between summer and winter at a
98 given latitude. The change in the seasonal difference in insolation then affects the oceanic and
99 atmospheric circulations, the amount of water evaporated above the ocean and precipitated
100 above the landmasses, the vegetation and ice covers, the sea level, the weathering intensity,

101 the detrital and nutrient supply to marine environments, the primary productivity, the redox
102 conditions and, finally, the preservation of organic matter (Strasser, 2006). All these orbital
103 imprints then may impact the petrophysical and mechanical properties of the sediment
104 deposited and influence the evolution of the sediment during the burial diagenesis.

105 Considering that both climate and sea-level oscillations are partly controlled by Milankovitch
106 cyclicity, we aim to decipher if the distribution and thickness of mineralized hydrofractures
107 (e.g., beef) in organic-rich sediments are indirectly forced by cyclic astroclimatic changes.

108 This hypothesis, if confirmed, could help predict the distribution of BPVs in organic-rich
109 mudrock using the well-calibrated record of astronomical cycles.

110 In the Vaca Muerta Fm. of the Neuquén Basin, sedimentological, mineralogical and chemical
111 studies pointed the role of the orbital forcing in humid/arid and sea-level cycles which
112 generated marl-limestone alternations (Scasso et al., 2005; Kietzmann et al., 2011, 2015). In
113 particular, annually humid conditions favoured detrital input to the basin and led to the
114 deposits of siltstone and claystone while limestone beds originate from the export of
115 carbonate mud to the basin under semi-arid conditions (Scasso et al., 2005; Rodriguez Blanco
116 et al., 2020). Humid conditions and increased nutrient input favoured, together with increased
117 sea level, the primary productivity in the basin and the preservation of organic matter (Scasso
118 et al., 2005; Kietzmann et al., 2015). The sedimentary record of orbital cycles has thereby
119 already been recognized in the Late Jurassic and Early Cretaceous deposits of the Neuquén
120 Basin from bed pattern, geochemistry, and magnetic susceptibility (Scasso et al., 2005;
121 Kietzmann et al., 2015; Kohan-Martinez et al., 2018; Kietzmann et al., 2018; Aguirre-Urreta
122 et al., 2019). The Neuquén basin appears especially suitable to investigate the relationship
123 between astroclimatic forcing and distribution/thickness of mineralized palaeo-hydrofractures.

124 To document this potential forcing, we revisited the Huncal section of the Upper Jurassic -
125 Lower Cretaceous Vaca Muerta Fm in the Neuquén Basin containing a high beef

126 concentration (Rodrigues et al., 2009; Larmier, 2020). This outcrop displays a continuous
127 sedimentary record composed of overmatured organic-rich black shales interbedded with
128 abundant bedding-parallel calcite veins (. A coupled analysis of sedimentary proxies and of
129 the palaeo-hydrofracturing signal has therefore been conducted using high-resolution
130 measurements of Magnetic Susceptibility (MS), Total Organic Carbon (TOC), mineralogical
131 (bulk and clay size fraction) and chemical composition together with beef distribution and
132 thickness. Spectral analyses have been applied to all proxies in order to test and compare their
133 potential cyclicity in relation with astronomical cycles and beef distribution/thickness and to
134 conclude about the impact of orbitally-driven climate changes on diagenesis and fracture
135 distribution in relation with the primary paleoenvironmental signal.

136

137 **2. Geological context**

138

139 *2.1. The Neuquén Basin*

140

141 The Neuquén Basin has a broadly triangular shape and is located in the Western part of
142 Argentina, in the foreland and foothills of the Andes (Fig. 1A) (Howell et al., 2005). The
143 Neuquén Basin was a retro-arc basin developed during the Mesozoic at the Pacific margin of
144 South America (Legarreta and Uliana, 1991). The basin is filled by an Upper Triassic to
145 Upper Cenozoic sedimentary succession that includes continental and marine siliciclastic
146 sediments, carbonates and evaporites deposited during the different stages of the basin
147 evolution. From the Upper Triassic to the Lower Jurassic deposits, narrow and isolated
148 depocentres composed of continental and volcanic deposits accumulated during the
149 extensional regime phase (Vergani et al., 1995; Franzese and Spalletti, 2001; Ramos et al.,
150 2019). From the Lower Jurassic to the Upper Cretaceous deposits, regional thermal

151 subsidence related to the subduction along the western margin of the basin is responsible for a
152 wide marine embayment (up to 4000 m deep) recorded as marine deposits that shallow up
153 eastwards and a fringe of continental deposits on the outer margin of the basin (Vergani et al.,
154 1995). From the Upper Cretaceous to the Upper Cenozoic deposits, a thick succession of
155 synorogenic continental sediments filled the basin during compressive deformation regime
156 (Legarreta and Uliana, 1991). This Andean deformation phase resulted in the development of
157 fold and thrust belts that exhumed Mesozoic succession throughout the basin (Fig. 1A).

158

159 *2.2. The Vaca Muerta Formation*

160

161 Outstanding Upper Jurassic to Lower Cretaceous outcrops are exposed in the basin, especially
162 in the western central part of the basin where the Tithonian-early Valanginian interval is
163 recorded through a sedimentary pile locally reaching 1500 m thick (Leanza et al., 2011). This
164 Upper Jurassic to Lower Cretaceous sequence is composed of transgressive-regressive
165 sequences that developed in response to variations in subsidence rate, eustatic fluctuations and
166 regional uplift (Legarreta and Gulisano, 1989; Kietzmann et al., 2014; Krim et al., 2017).
167 These marine sequences are included in the Mendoza Group (also referred to as Mendoza
168 Mesosequence) (Fig. 1C). Legarreta and Gulisano (1989) divided the Mendoza Group into
169 three shallowing upward sedimentary sequences: the lower Mendoza Subgroup
170 (Kimmeridgian–Lower Valanginian), the middle Mendoza Subgroup (Upper Valanginian–
171 Lower Hauterivian) and the upper Mendoza Subgroup (Upper Hauterivian–Lower
172 Barremian). The lower Mendoza Subgroup, object of the present study, records the
173 continental deposits of the Tordillo Formation (Kimmeridgian-lower part of the Lowermost
174 Tithonian) and the thick deep marine deposits of the Vaca Muerta Fm (upper part of the
175 Lower Tithonian - Upper Berriasian to Lower Valanginian) (Figs. 1B, C). In most areas of the

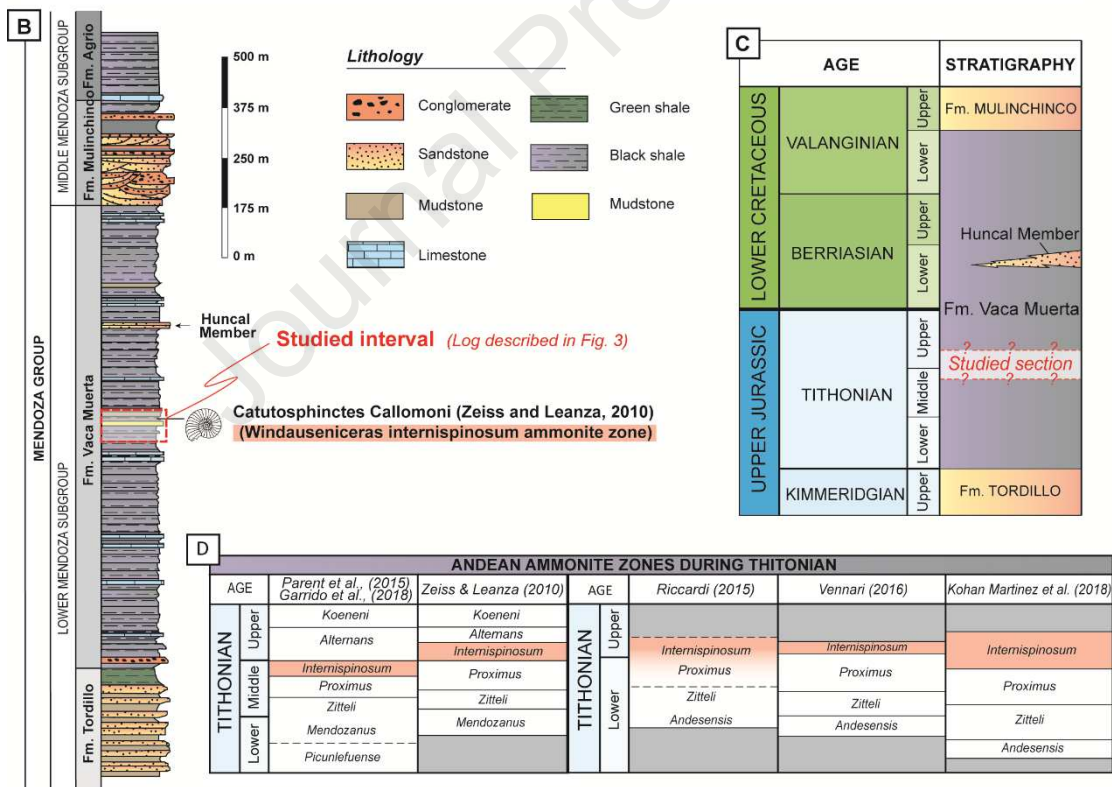
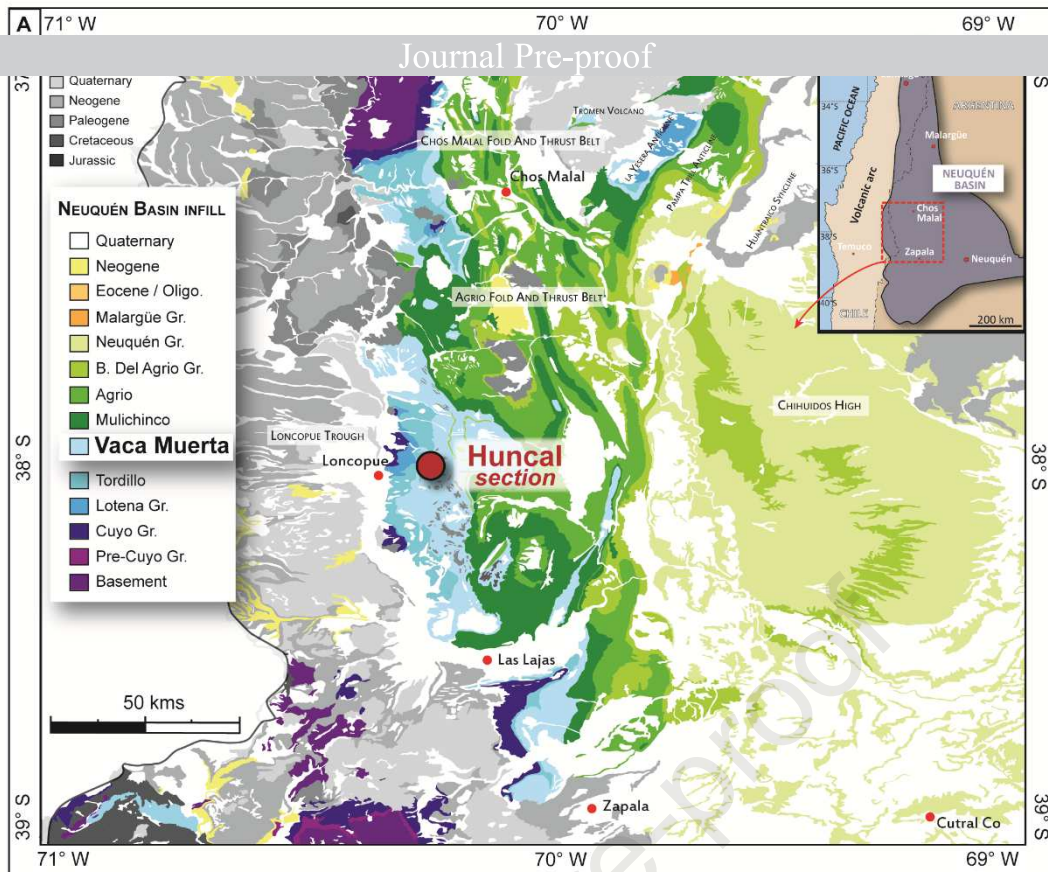
176 Neuquén Basin, the Vaca Muerta Fm corresponds to dark and organic-rich mudrocks, marls
177 and limestones deposited along a homoclinal ramp flooded by a marine transgression
178 originating from the Pacific Ocean (Kietzmann et al., 2014). The Vaca Muerta black shales
179 are basinal ramp facies considered as a world-class source rock (with TOC values ranging
180 from 2 to 12%) of high unconventional hydrocarbon potential . The Vaca Muerta Fm is
181 diachronous as the top becomes younger toward the central part of the basin (Leanza et al.,
182 2003). In the western part of the Vaca Muerta Fm, a Lower Berriasian turbiditic sandstone
183 interval referred to as the Huncal Member is a useful stratigraphic marker (Leanza et al.,
184 2003) (Figs. 1 B, C; 2A).

185

186

187

188



189 **Figure 1.** (A) Geological map of the eastern central part of the Neuquén Basin with location of the Huncal
 190 section. (B) Section of the Vaca Muerta Fm in the Huncal area (modified after Leanza et al., 2003) with a focus
 191 on the position of the sedimentary interval described in this study. (C) Lithostratigraphic framework of the Vaca
 192 Muerta Fm in the Huncal area (modified after Leanza et al., 2011). (D) Chart of the Tithonian ammonoid
 193 biostratigraphy for the Andean region based on multiple studies conducted in the Neuquén Basin.

194

195 *2.3. The Huncal section*

196

197 The section investigated in this study, belonging to the Vaca Muerta Fm, is located near the
198 locality of Huncal, along the Huncal river, a few kilometers southeast of Cerro Mulinchinco
199 ($38^{\circ}06.242'$ S; $70^{\circ}35.847'$ W) (Fig. 1A). A synthetic log of the Huncal area has been
200 realised by Leanza et al. (2011), where a complete 1150 m thick section of the Vaca Muerta
201 Fm is reported (Fig. 1B). Leanza's work conducted in this area refers to a beef-rich interval
202 approximately 250 m beneath the Huncal Mb, especially in the area of Cerro Mulinchinco
203 (Leanza et al., 2003, 2011). We studied a 102 m thick and continuous section that shows a
204 very high beef concentration we highly suspect to be the equivalent of the "shales with beef"
205 interval described in Leanza et al. (2011). The beef-rich section we investigated is beneath the
206 Huncal Mb (Figs. 1B, C; 2A). Ammonites are commonly found along the section and best
207 preserved in bedding-parallel calcite veins (Rodrigues et al., 2009). Although mostly
208 degraded, one ammonite specimen identified in the uppermost part of the section corresponds
209 to *Catutosphinctes Callomoni* (H. Leanza pers. comm.) (Figs. 1B, 2C; 3). According to Zeiss
210 and Leanza (2010), this species is characteristic of the *Windausenicerias internispinosum*
211 Andean ammonite Zone, indicating a Middle to early Upper Tithonian age (Fig. 1D).
212 Recently, astronomical calibration of the Tithonian-Berriasian conducted in the Neuquén
213 Basin has estimated to 1.21 myr the duration of the *W. internispinosum* Zone (Kietzmann et
214 al., 2018).

215

216 *2.4 Bedding-parallel calcite veins (beef) in the Huncal area*

217

218 BPV or beef have been largely studied in the Vaca Muerta Fm due to their widespread
219 occurrence in the Neuquén Basin (Rodrigues et al., 2009; Gale et al., 2014; Zanella et al.,

220 2015b; Eberli et al., 2017; Lejay et al., 2017; Ukar et al., 2017; Weger et al., 2019). Typical
221 veins are composed of fibrous calcite perpendicular to bedding that are either continuous,
222 discontinuous or lens-shaped. They commonly display several generations of calcite
223 crystallisation related to several phases of hydrofractures opening along a single mechanic
224 interface. The inner generations are generally grey, as a result of numerous inclusions of wall
225 rock and hydrocarbons. The outer generations are white, because of a lack of these inclusions.
226 A median line or zone appears between the inner zones. This line also contains abundant
227 inclusions of wall rock (Rodrigues et al., 2009). From burial curves, maturity calculations,
228 growth strata, and ages of igneous intrusions, Rodrigues et al. (2009) estimated that the inner
229 generation of the beef formed when the formation reached the oil window during the Aptian-
230 Albian. Conversely, the outer generation formed when the formation reached the gas window
231 during the Cenomanian-Campanian. Their formation is attributed to organic matter abundance
232 in black shales and fluid overpressure development during chemical compaction and
233 transformation of solid kerogen into oil or gas (Rodrigues, 2009). Larmier (2020)
234 demonstrated the link between TOC and beef characteristics along the studied section by
235 showing highest density of beef in sedimentary intervals displaying higher TOC values.
236 Nevertheless, this relationship between TOC and beef occurrence is not always recorded in the
237 basin (Weger et al., 2019).

238

239 **3. Materials and Methods**

240

241 *3.1. Sampling and methodology for beef position and thickness*

242

243 We conducted a high-resolution sedimentary logging and sampling along a 100 m thick
244 section in the Huncal area. Using a Jacob's staff, a 1:10 sedimentary logging has been carried

245 together with an even sampling step of 10 cm (1000 samples in total). Beef layers and
246 dolostone beds were discarded from the measurement of the sampling distances to only
247 sample shales and eliminate any bias in the physical and chemical signals acquired. In
248 parallel, maximum thickness and lateral continuity of every beef have been measured. The
249 outcrop generally offered tens of meters long viewing of single beef, a rough estimation of the
250 degree of continuity was therefore performed by observing their lateral continuity at outcrop
251 scale. Continuous beef at outcrop scale were therefore labelled as “continuous” while beef
252 with poor lateral continuity or lens-shaped were labelled as “discontinuous”. Diffuse beef less
253 than a millimeter-thick, referred to as “microbeef” in some studies (Lejay et al., 2017;
254 Larmier, 2020) were very difficult to fully characterize and were therefore not measured.

255 To quantify the beef signal along the section, we extracted three signals from the beef
256 database: (1) beef occurrence, (2) beef median line position and (3) beef thickness. (1) Beef
257 occurrence corresponds to the beef presence or absence for every single millimeter of the
258 section. A value of 1 is attributed to the presence of beef while a value of 0 corresponds to
259 mm-thick intervals devoid of beefs. (2) The beef median line position corresponds to the
260 position of the median line (Fig. 4B) of every single beef described along the section. (3) The
261 beef thickness signal required an additional operation to be independent from the occurrence
262 or median line signals described above. The beef thickness values are resampled every 10 cm
263 along a curve constituted by a point-to-point linear interpolation between thickness values
264 recorded for every beef position. As the very few thick beefs occurring in beef-poor intervals
265 bring a substantial bias in the interpolation curve (see section 4.7), we built an additional
266 curve where they have been removed.

267

268 *3.2. Magnetic Susceptibility*

269

270 Magnetic susceptibility (MS) was measured on the 1000 bulk shale samples collected every
271 10 cm along the section to analyse the evolution of the detrital export along the section.
272 Usually, iron bearing minerals have higher magnetic susceptibility values than non-iron
273 bearing minerals. As the iron is exported to the basin from the continental erosion and
274 weathering, MS measurements will help deciphering the impact of the Milankovitch cycles on
275 the detrital export. MS values were acquired using a laboratory Agico Kappabridge KLY-3S
276 samples (Geosciences Rennes, Université Rennes 1). Volumic MS was measured three times
277 and corrected from measurements of volumic MS performed on empty containers. Sample
278 values, corrected from blanks, were normalized to the measurement volume and the sample
279 mass and given in m^3/kg .

280

281 *3.3. Total Organic Carbon*

282

283 We used 198 samples collected for MS measurements for to TOC measurements (in %
284 weight) following an even sampling step of 50 cm. Both organic carbon content and thermal
285 maturation of the organic matter were measured using a Rock-Eval instrument (Rock-Eval 6
286 Turbo device; Vinci Technologies). TOC results from this sampling series along the Huncal
287 section have already been published in Larmier (2020).

288

289 *3.4. X-ray diffraction*

290

291 X-ray diffraction (XRD) analyses were conducted on 30 shale samples every 3 meters along
292 the section to obtain the whole mineralogical composition. The first 33 meters, corresponding
293 to a beef-rich stratigraphic interval (Fig. 3), has been selected for higher resolution XRD
294 analyses with samples measured every 30 cm (100 samples in total).

295 Each sample was cleaned, crushed and finely powdered using a metal ring grinder.
296 Diffractograms were obtained using a Bruker D4 Endeavor diffractometer with $\text{CuK}\alpha$
297 radiations, LynxEye detector and a Ni filter, under 40 kV voltage and 25 mA intensity
298 (Biogéosciences Laboratory, Université Bourgogne Franche-Comté). The goniometer scanned
299 the sample from 2.5° to 30° for each run showing diffraction peaks for every crystalized
300 mineral phase.

301 Minerals phases were identified by the position of their main diffraction peaks while semi-
302 quantitative estimates were produced in relation to their area (Moore and Reynolds, 1997).
303 Areas were determined on diffractograms with MacDiff 4.2.5 software (Petschick, 2000).
304 Beyond the evaluation of the absolute proportions, the objective is to identify their relative
305 fluctuations along the section. Peak area ratios were then considered for time series analyses.
306 Clay mineral identification and semi-quantification were also performed on the decarbonated
307 clay-sized fraction ($<2\mu\text{m}$) using a 0.2 M HCl solution. Three runs were performed for each
308 sample to discriminate clay phases using oriented glass slide preparation: 1) air-drying; 2)
309 ethylene-glycol solvation; 3) heating at 490°C . Clay minerals were identified using their
310 main diffraction (d_{001}) peak and by comparing the three diffractograms obtained while
311 quantification was obtained on ethylene-glycol solvation runs (Moore and Reynolds, 1997).
312 Calcite percentages obtained from XRD measurements were calibrated by calcimetry
313 measurements (Bernard calcimeter, Biogéosciences Laboratory, Université Bourgogne
314 Franche-Comté).

315

316 *3.5. X-ray fluorescence*

317

318 X-ray fluorescence (XRF) analyses were conducted on 100 samples taken every 30 cm along
319 the first 33 meters of the section. Each sample was turned into powder and analysed using a

320 hand XRF S1 Titan Bruker (Biogéosciences Laboratory, Université Bourgogne Franche-
321 Comté) to identify and quantify major element composition. Analyses of the elementary
322 composition of the shales have been focus on several ratios of chemical elements relevant for
323 approaching the changes in the terrigenous flux (Ti, Fe, Si, Al, K) and indirectly in the grain-
324 size as Si is normally enriched in the silt size fraction and Al and K are commonly enriched in
325 the clay size fraction. We therefore selected the following ratios: Si/Al, Ti/Al, Ti/K and Fe/Al
326 as sedimentological and environmental proxies.

327

328 *3.6. Spectral analyses*

329

330 Frequency content analyses were performed using the multi-taper method (MTM; Thomson,
331 1982, 1990) applying three 2π -tapers (2π -MTM spectra). The confidence levels of the spectral
332 peaks were extrapolated assuming a chi-square distribution of the red-noise fit of the spectral
333 background calculated according to the method of Mann and Lees (1996) implemented in
334 Meyers (2014). The spectra are given with a Rayleigh frequency (frequency resolution of the
335 spectrum) of $0.0099 \text{ cycles.m}^{-1}$. Filters were then calculated using Taner filters (see
336 supplementary material in Hinnov et al., 2002 for technical details of the filter). The
337 sedimentation rate was then calculated per each repetition of the filter of the precession cycle
338 by dividing the thickness of a cycle by the average duration of the precession cycles ($20.2 \pm$
339 0.5 kyr ; Waltham, 2015). We assume that the sedimentation rates are constant within a
340 precession cycle. The TOC series was used as the reference for the precession filter as this
341 series was regularly sampled and shows high amplitude of the filter of the precession
342 throughout the interval studied.

343

344 **4. Results**

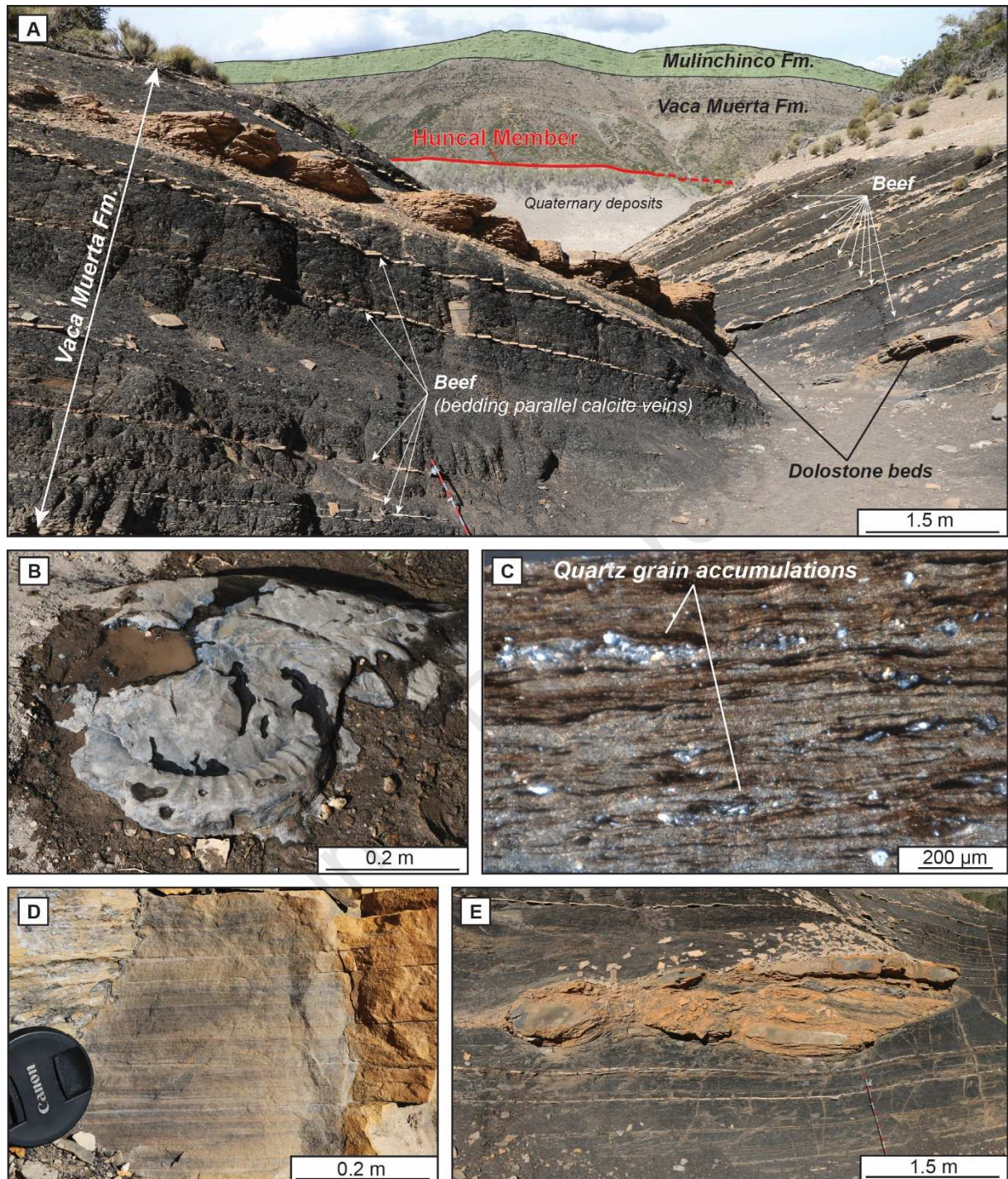
345

346 *4.1. The Huncal section deposits*

347

348 The section is predominantly composed of black shale deposits interrupted by several
349 dolostone interbeds (Figs. 2A, 3). Shale contain abundant ammonites, best preserved in beef
350 and microfossils including radiolarian and coccolithophores. Accumulations of silt-sized
351 quartz grains forming microscopic beds parallel to layering are commonly observed in shale
352 (Fig. 2C). We reported 11 orange-colored competent dolostone beds with sharp contacts
353 ranging from 0.2 m to 1 m thick, which accounts for 5% of the section thickness. Their
354 microfacies is often characterized by an equigranular mosaic of anhedral to subhedral
355 dolomite crystals, probably formed by the postdepositional diagenesis. This early diagenesis

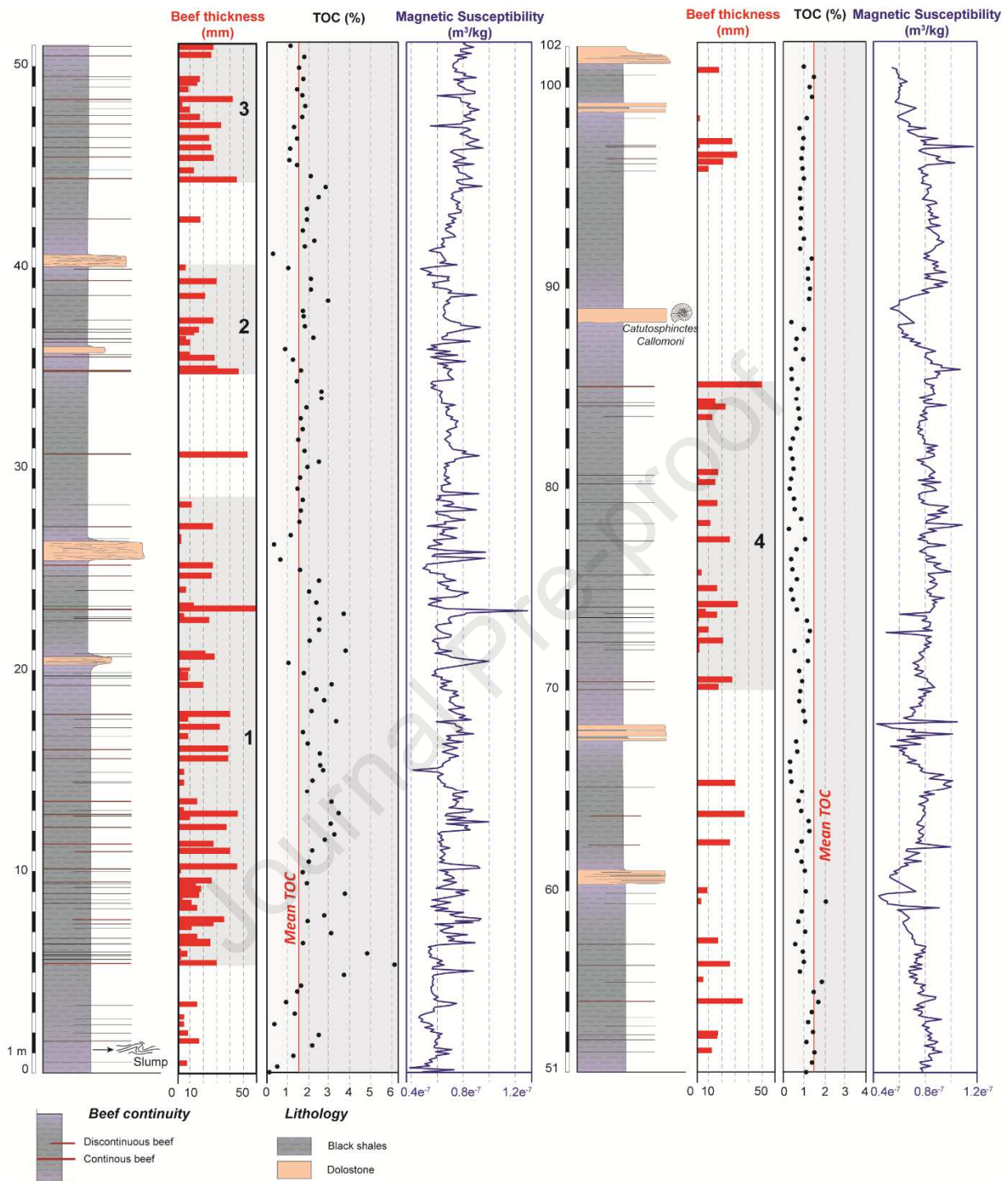
356



357

358 **Figure 2.** (A) Typical aspect of the Hunca section where multiple bedding parallel calcite veins (beef) set in the
 359 organic-rich mudrock of the Vaca Muerta Fm. Dolostone beds locally interrupt the mudrock lithology. Note the
 360 Hunca member position in the upper part of the Vaca Muerta Formation in the background. (B) Ammonite
 361 (*Catulosphinctes Callomoni*) found in a dolostone bed (89 meters). (C) Microscopic view of thinly laminated
 362 mudrocks displaying micro-beds composed of silt-sized quartz grains. (D) Thinly laminated dolostone beds that
 363 sometimes show faint current ripples. (E) Slump deposits in the Vaca Muerta Fm.

364



365

366 **Figure 3.** Sedimentary log of the Huncal section with distribution, thickness and continuity of the beef. TOC
 367 values (measured every 50 cm) and MS values (measured every 10 cm) are reported along the section. Shaded
 368 intervals labelled 1 to 4 correspond to beef-rich intervals mentioned in the text.

369

370 provides a good preservation of mudstone primary fabric including thinly laminated beds and
371 occasional faint current ripples (Fig. 2D). Thin laminations and current sedimentary structures
372 in a basinal sedimentary succession suggest that dolostones were deposited by very fine-
373 grained sedimentary density flow (Fig. 2B). These beds could either represent the distal part
374 of dilute gravitational flows, perhaps induced by storm surges, turbidites or long-lived muddy
375 hyperpycnal flow originating from the reworking of inner ramp sediments (Spaletti et al.,
376 2000; Blanco et al., 2020) or triggered by extreme river discharges (Otharan et al., 2020). The
377 occurrence of slump deposits at the base of the section (1.2 m) (Fig. 2E) strengthens a gravity-
378 induced origin for these thinly laminated dolostone beds.

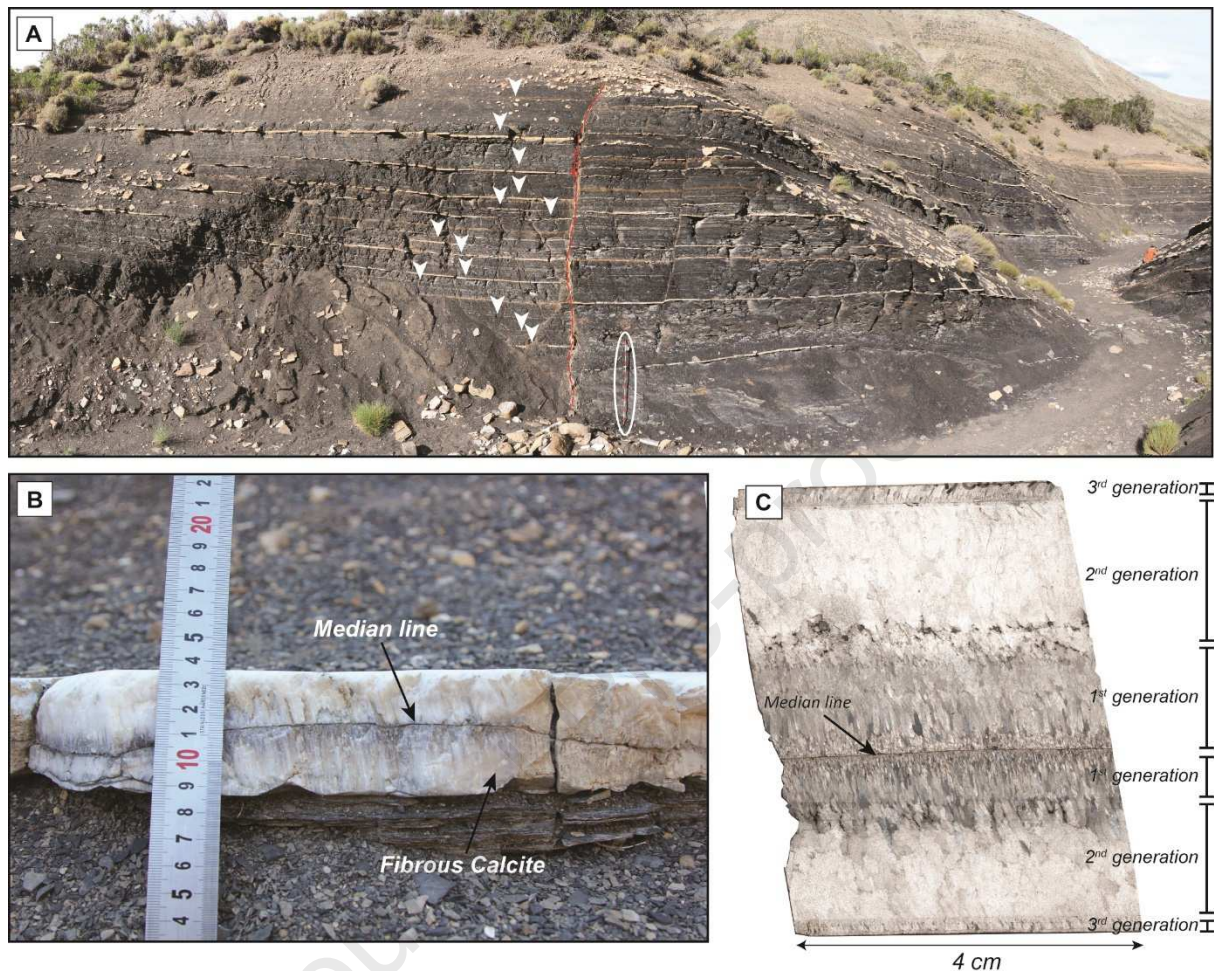
379

380 *4.2. Beef distribution and thickness*

381

382 Along the section, 135 beef layers have been measured with thickness ranging from 1 to 62
383 mm (mean thickness: 18 mm) and lateral extent ranging from few meters to tens of meters
384 (Fig. 4A). The cumulated beef thickness accounts for around 4 % of the total thickness of the
385 102 m thick interval. We measured 16 beef layers comprised between 0 and 2 mm thick, 32
386 beef between 2 and 10 mm, 34 between 11 and 20 mm, 33 between 21 and 30 mm, 12
387 between 31 and 40 mm, 7 between 41 and 50 mm and only two being superior to 50 mm thick
388 (Fig. 3). The beef distribution is not homogeneous but clustered in four main stratigraphic
389 intervals ranging from 5 meters up to 26 meters thick (labelled 1 to 4 on Fig. 3). A denser beef
390 proportion is observed in the first 50 meters where the thickest beef layers have also been
391 measured. The first beef-rich interval (5 to 27 meters) gathers 45% of all beef measured along
392 the section (n=61 beef) (Fig. 3). We also observe that intervals with low beef concentration
393 show a few thick beef layers (30.73 m 34.87 m, 62.28 m, 63.74 m, 65.22 m and 85.1 m) (Fig.

394 3). All beef layers show a median line and one to several generations of fibrous calcite
 395 crystallisation (Figs. 4B, C).



396
 397 **Figure 4.** (A) Beef-rich intervals in the lower part of the Huncal section (5 to 10 m). White arrows point beef.
 398 Note 1.5 m Jacob's staff as scale. (B) Close-up on beef structure where a median line separates two sets of
 399 antitaxial fibrous calcite. (C) Thin section showing beef internal structure characterised by distinctive zones
 400 related to several generation of fibrous calcite precipitation. The first generation is greyer due to hydrocarbon
 401 and wall rock inclusion.

402

403 4.3. Total Organic Carbon

404

405 TOC values along the section range from 0.1 to 6.1% along the section with an average of
 406 1.5% for the 250 samples measured (Fig. 3). The highest TOC values are measured in the first
 407 43 meters where TOC values are mostly above mean TOC. Beef-rich intervals 1 to 3

408 generally coincide with higher TOC values (Fig. 3). In the first 33 meters of the section, the
409 occurrences of the thickest beef layers coincide with TOC values above average (Fig. 5).

410

411 *4.4. Magnetic Susceptibility*

412

413 MS values range from $0.346 \cdot 10^{-7}$ to $1.583 \cdot 10^{-7}$ m³/kg with an average of $0.734 \cdot 10^{-7}$ m³/kg.

414 Mean MS values generally increase in beef-rich intervals and seem to be correlated with the
415 occurrence of thickest beef (Fig. 3, 5).

416

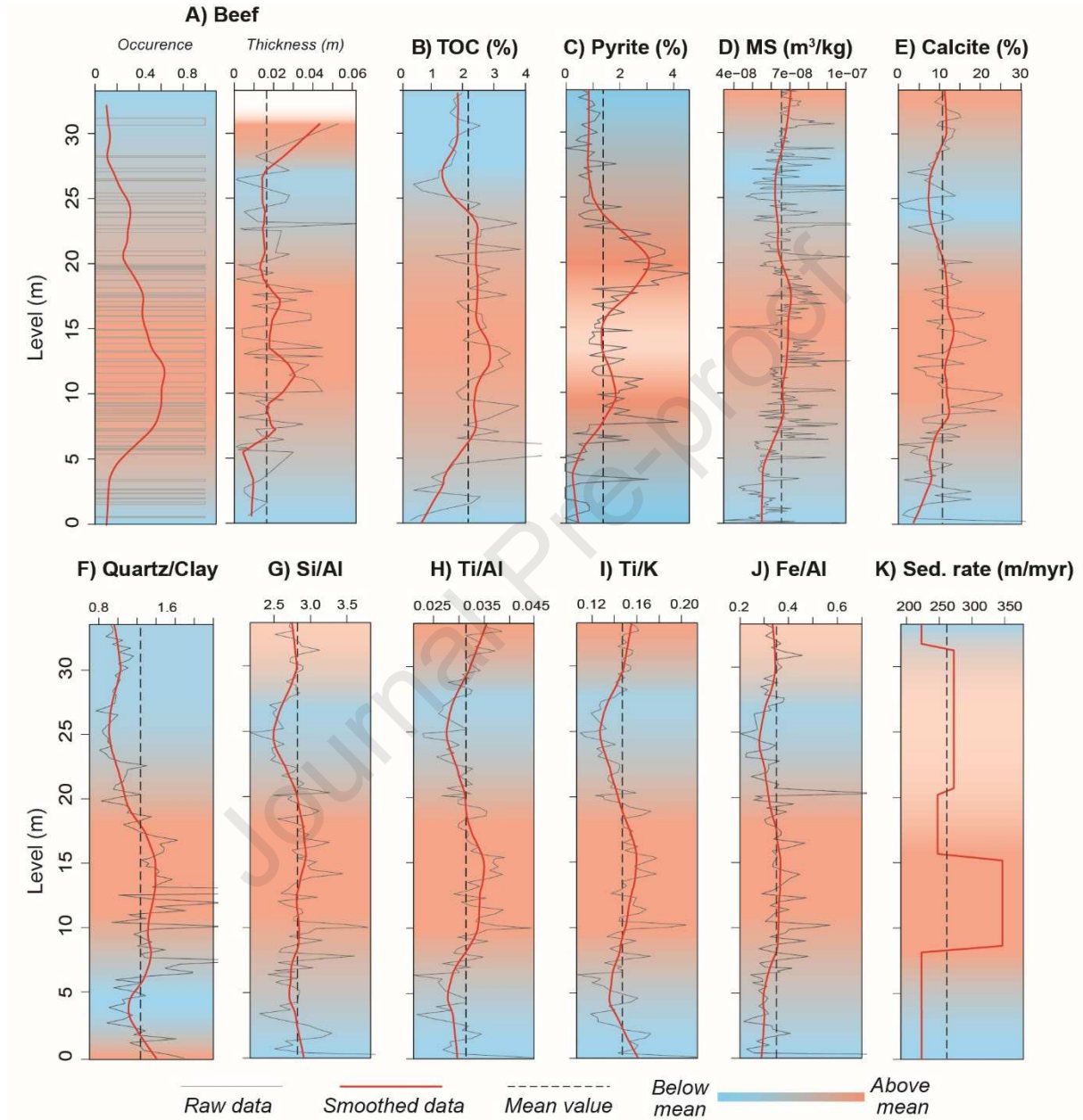
417 *4.5. Mineralogy of the black shale deposits*

418

419 X-ray diffraction analyses realized on 125 black shale samples show a mean mineralogical
420 composition characterized by 61% of quartz, 14% of albite, 12 % of clay, 10% of calcite, 2 %
421 of pyrite and less than 1% of gypsum. Calcite percentages obtained from XRD measurements
422 were calibrated by calcimetry measurements. Detailed mineralogical analyses performed in
423 the first 33 meters of the section show similar trend between the Quartz/Clay ratio, used here
424 as a detrital proxy, and the calcite content. The Quartz/Clay ratio displays higher values from
425 6 to 18 meters (from 1.2 to 1.4; Fig. 5F) while calcite content is the highest between 7 and 20
426 meters (11 to 14%; Fig. 5E). These two proxies coincide with higher TOC values (2.4% on
427 average) and denser beef distribution (Fig. 5). Pyrite content (ranging from 0 to 22%; 1.3% on
428 average) also displays higher values between 8 and 23 meters with two local maxima around
429 10 and 20 meters. Clay mineral assemblages show on averages 59% of R3 type illite/smectite
430 mixed-layers (IS R3), 27% of illite, 10% of chlorite and 4% of complex chlorite-vermiculite-
431 smectite mixed-layers. The high proportion of IS R3 (composed of 90% of illite sheets) and

432 illite indicate that sediments have experienced significant burial diagenesis with a maximal
 433 burial temperature of 190°C (Šucha et al.,1993).

434



435

436 **Figure 5.** Evolution of the beef occurrence and thickness, the TOC (every 50 cm), the mineralogical content
 437 (Pyrite, Calcite, and Quartz/Clay) and some key ratio of chemical elements (every 30 cm). The sedimentation
 438 rate for the first 33 meters of the Huncal section is deduced from the thickness of the precession cycles (cf.
 439 section 5.1). Raw and smoothed data are shown for each plot.

440

441

442

443

444 *4.6. Geochemistry of the black shale deposits*

445

446 The Si/Al, Ti/Al, Ti/K and Fe/Al ratios display very similar evolution with values above mean
447 reached within the 8 to 19 meters and 29 to 33 meters intervals and below mean in the 0 to 8
448 and 19 to 29 meters intervals (Fig. 5). This evolution positively correlates with other proxies
449 analysed in the first third of the studied section (i.e., beef occurrence and thickness, TOC, MS,
450 Calcite, Quartz/Clay and sedimentation rate).

451

452 *4.7. Spectral analyses*

453

454 The 2π -MTM spectra of the MS, TOC, Beef Occurrence (BO) and Median Beef Position
455 (MBP) series all show three groups of spectral peaks at the following frequencies (Figs. 6, 7
456 and 8):

457 (i) 0.0297 to 0.0396 ± 0.0099 cycles.m⁻¹ (corresponding periods: 34 to 25 m),

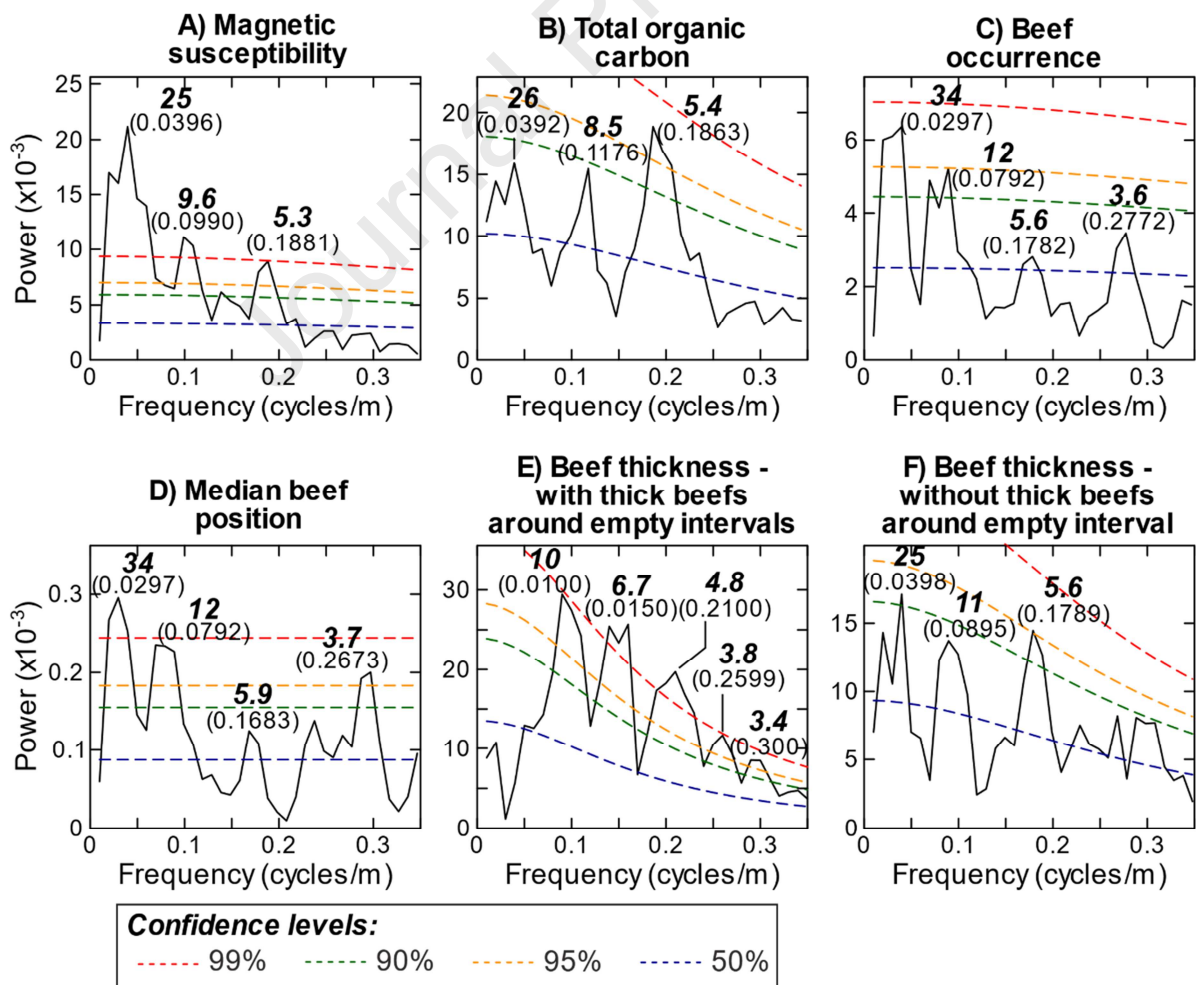
458 (ii) 0.0792 to 0.1275 ± 0.0099 cycles.m⁻¹ (corresponding periods: 12 to 8.5 m),

459 (iii) 0.1683 to 0.1881 ± 0.0099 cycles.m⁻¹ (corresponding periods: 5.9-5.3 m).

460 The average frequency of these three groups are 0.0346, 0.0938 and 0.1802 cycles.m⁻¹,
461 respectively corresponding to periods at 28.9 m, 10.7 m and 5.5 m. Other spectral peaks are
462 observed in the BO and the MBP series respectively at frequencies 0.2772 cycles.m⁻¹ (period:
463 3.6 m) and 0.2673 cycles.m⁻¹ (period: 3.7 m) (Figs. 6C, 6D and 8).

464 The 2π -MTM spectrum of the Beef Thickness (BT) series shows a group of spectral peaks
465 with decreasing powers from frequencies 0.0100 to 0.300 cycles.m⁻¹ (corresponding periods:

466 from 10.0 m to 3.4 m) (Fig. 6E). At ~30 m, ~60 m and ~90 m, few but thick beef layers are
 467 recorded around intervals devoid of beef (see red circles in Fig. 8C), locally creating
 468 sequences of high amplitudes. This feature makes the beef thickness series unstationary and
 469 biases the spectrum (Weedon, 2003). Interestingly, this pattern occurs recurrently every ~30
 470 m, which corresponds to the longest period observed in the other spectrograms. To overcome
 471 this bias, we removed the very thick beefs directly surrounding the intervals devoid of beefs.
 472 The beefs discarded from the further analysis are shown as red circles in Figure 8C.
 473 The 2π -MTM spectrum of the BT series without the thick beefs around the intervals devoid of
 474 beefs shows spectral peaks at frequencies 0.0398, 0.0895, 0.1789 cycles.m⁻¹, respectively
 475 corresponding to 25 m, 11 m and 5.6 m (Fig. 6.F). These periods agree with the periods found
 476 in the spectra of the MS, TOC, BO and MBP.

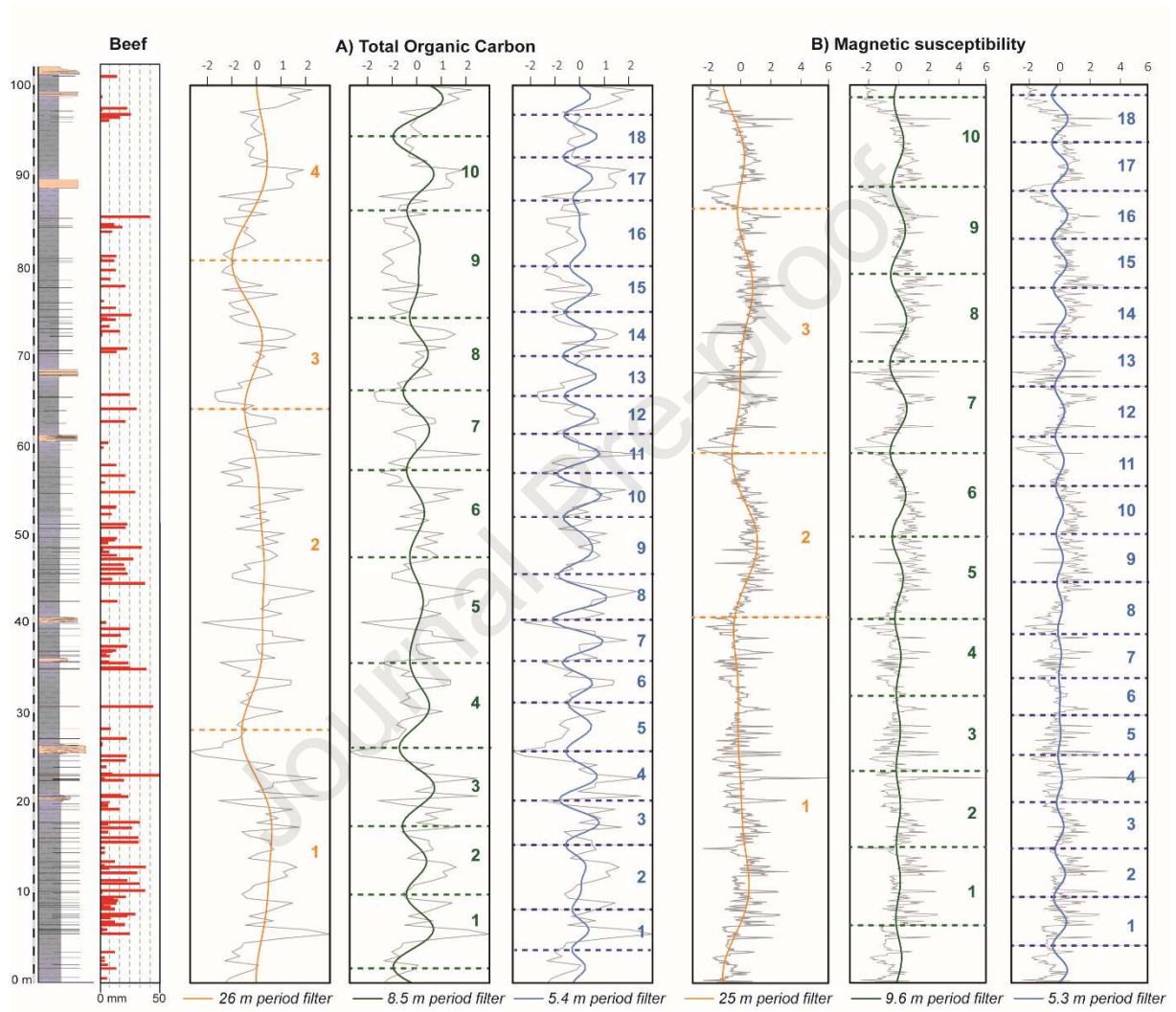


477
 478

479 **Figure 6.** 2π -MTM spectra of the series measured throughout the entire studied series. Periods of the spectral
 480 peaks in meters are labelled bold and are in meters. The corresponding frequencies are labelled in between
 481 brackets and are in cycles/m.

482

483



484

485 **Figure 7.** Taner filters of the Total Organic Carbon (TOC) and the Magnetic Susceptibility (MS) series.

486

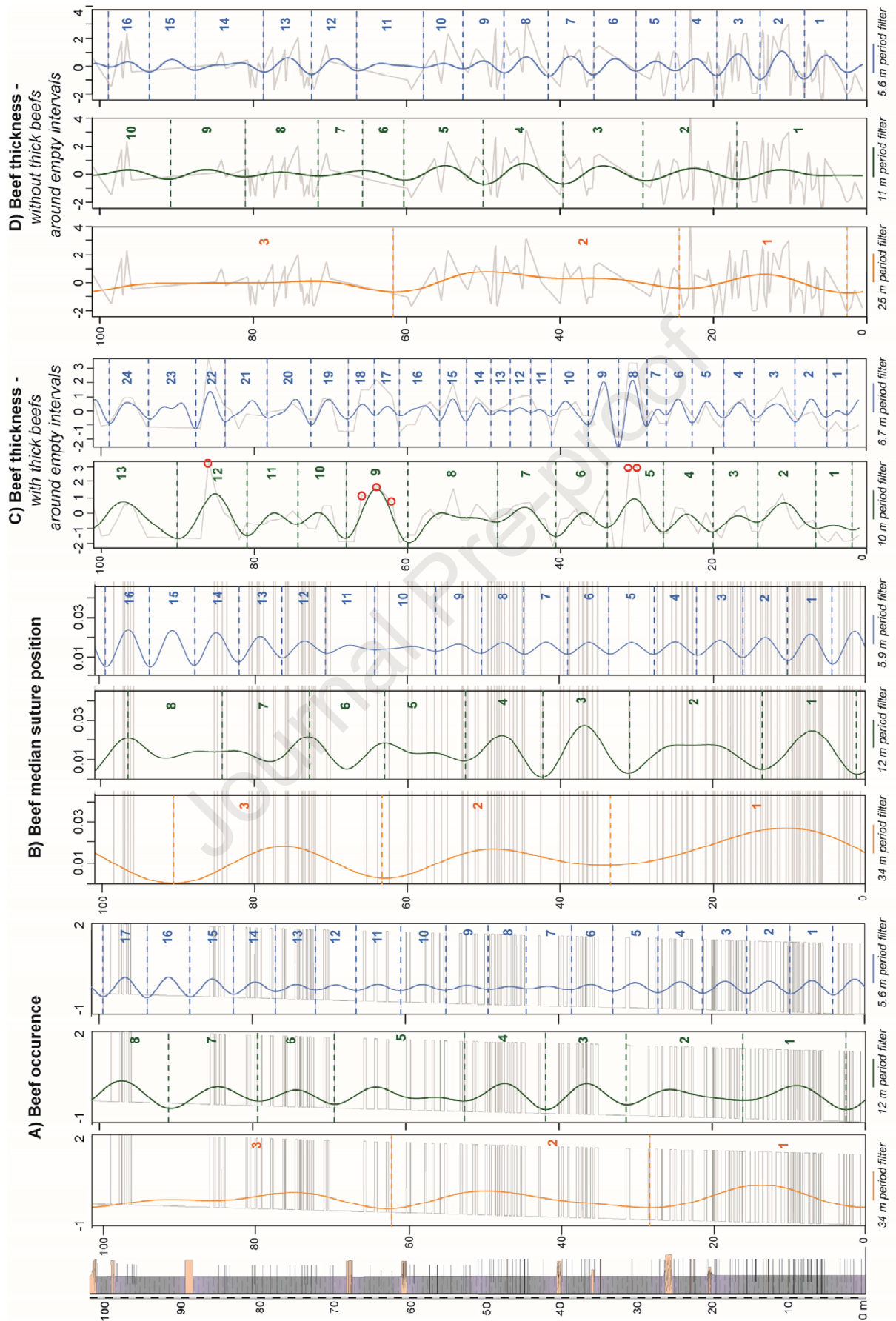
487

488

489

490

491



492

493 *Figure 8. Taner filters of the beef-related series.*

494

495 **5. Discussion**

496

497 *5.1 Significance of the sedimentary cycles*

498

499 The series of MS, TOC, BO, MBP and BT (without thick beef around intervals devoid of
500 beefs) all display peaks at 25-34 m, 8.5-12 m and at 5.3-5.9 m (Figs. 6, 7 and 8). The
501 difference in the period of the signals is due to the discretisation of the spectra, which is
502 inherent to spectral analyses performed on finite series (Weedon, 2003). This effect is
503 particularly obvious for the longest period, where the ~30 m peak has a period ranging from
504 25 to 34 m depending on the proxy analysed. These peaks have frequencies ranging from
505 $0.029 \text{ cycles.m}^{-1}$ (34 m) to $0.039 \text{ cycles.m}^{-1}$ (25 m). The difference of $0.01 \text{ cycles.m}^{-1}$ between
506 these two frequencies corresponds to the frequency resolution of the spectra shown here.

507 On average, three periods are commonly observed between these five above-mentioned
508 proxies, at 28.1 m, 10.8 m and 5.6 m. The ratio between these periods is 1.9:2.6:5.0, in perfect
509 agreement with the ratios between the periods of 100 kyr (eccentricity), 38.1 kyr (obliquity)
510 and 20.2 kyr (average precession) (Waltham, 2015). The observed periods of ~28 m, 11 m
511 and 5.6 m are thus respectively associated to the eccentricity, the obliquity and the precession,
512 which appears to influence both the lithological characteristics (TOC, MS) and mineralization
513 produced during diagenesis (beef distribution and thickness) of the Vaca Muerta deposits.

514 The spectrum of the BT does not show these periods when including the thick beefs around
515 intervals devoid of beefs (Fig. 6E). However, as demonstrated in section 4.2, this series is
516 biased as it only shows high powers localised at intervals where few but thick beefs occur. It
517 is noteworthy that these thick beef intervals occur every ~30 m, which corresponds to the
518 100-kyr eccentricity in the spectra of TOC, MS, BO and MBP. This shows that eccentricity

519 cycles impacted mudstone properties, so that it favoured the generation of thick, isolated beef
520 layers in organic-depleted intervals. After removing these beefs at 30.73 m 34.87 m, 62.28 m,
521 63.74 m, 65.22 m and 85.1 m (see red circles in Fig. 8C), the spectrum of the BT series
522 displays the same peaks at 25 m, 11 m and 5.6 m observed in the other proxies and related to
523 the imprint of the eccentricity, obliquity and precession, respectively. Notice that the different
524 beef signals display other peaks at 3-4 m which are not observed in the MS or TOC signals.
525 As they are not observed in other environmental proxies, these short periods observed in the
526 beef-related series are likely due to specific burial and diagenetic processes rather than the
527 imprint of an environmental change.

528

529 *5.2. Astroclimatic fingerprint and beef distribution model*

530

531 Detailed mineralogical and chemical analyses performed along the Huncal section show that
532 increasing beef density and thickness correlate with higher MS, TOC, calcite content, silt-to-
533 clay ratios and sedimentation rate (Fig. 5). This correlation suggests a link between the
534 primary sedimentary signal, diagenesis and hydrofracturing distribution in the mudrocks of
535 the Vaca Muerta Fm. Similar relationships have been proposed by other studies focusing on
536 the mechanisms of beef formation (Rodrigues et al., 2009; Zanella et al., 2015; Meng et al.,
537 2017; Larmier, 2020) although astroclimatic precursors have hitherto remained unexplored.

538 Based on spectral analyses, we demonstrate the influence of the orbital parameters as a
539 precursor for variations in both sedimentary signals (MS, TOC) and diagenetic features
540 (beef). Beef distribution can therefore be deciphered by considering the evolution of the
541 sedimentary record in view of climatic and/or eustatic fluctuations inferred from orbital
542 parameters.

543 Krim et al. (2017, 2019) suggested that grain-size and clay mineralogy variations observed in
544 the southern part of the Neuquén Basin during deposition of Vaca Muerta Fm can be
545 considered as a climatic imprint rather than a response to eustatic variations. Warm temperate
546 conditions associated with seasonal rainfall and increase runoff are proposed to explain the
547 increase of siliciclastic supply recorded in the Vaca Muerta mudrocks (Scasso et al., 2005;
548 Krim et al., 2019). Clay mineralogy is commonly used as a proxy for climatic reconstructions
549 (humidity/aridity) in the Late Jurassic (Hallam 1993; Pellenard & Deconinck 2006; Pellenard
550 et al., 2014; Turner & Huggett 2019) and was used in this way at a regional scale for the Vaca
551 Muerta Fm (Krim et al., 2019). Unfortunately, temperatures reached by the Huncal section
552 during the burial diagenesis ($\sim 190^{\circ}\text{C}$; Mean $T_{\text{max}} = 590^{\circ}\text{C}$) strongly affected mineralogy of
553 clays, mainly composed of illite, IS R3 and chlorite, preventing the use of clay minerals as
554 proxy of climate and comparison with the paleoenvironmental signal deduced from the south
555 of the Neuquén Basin (i.e., Huincul Arch area; Krim et al., 2019).

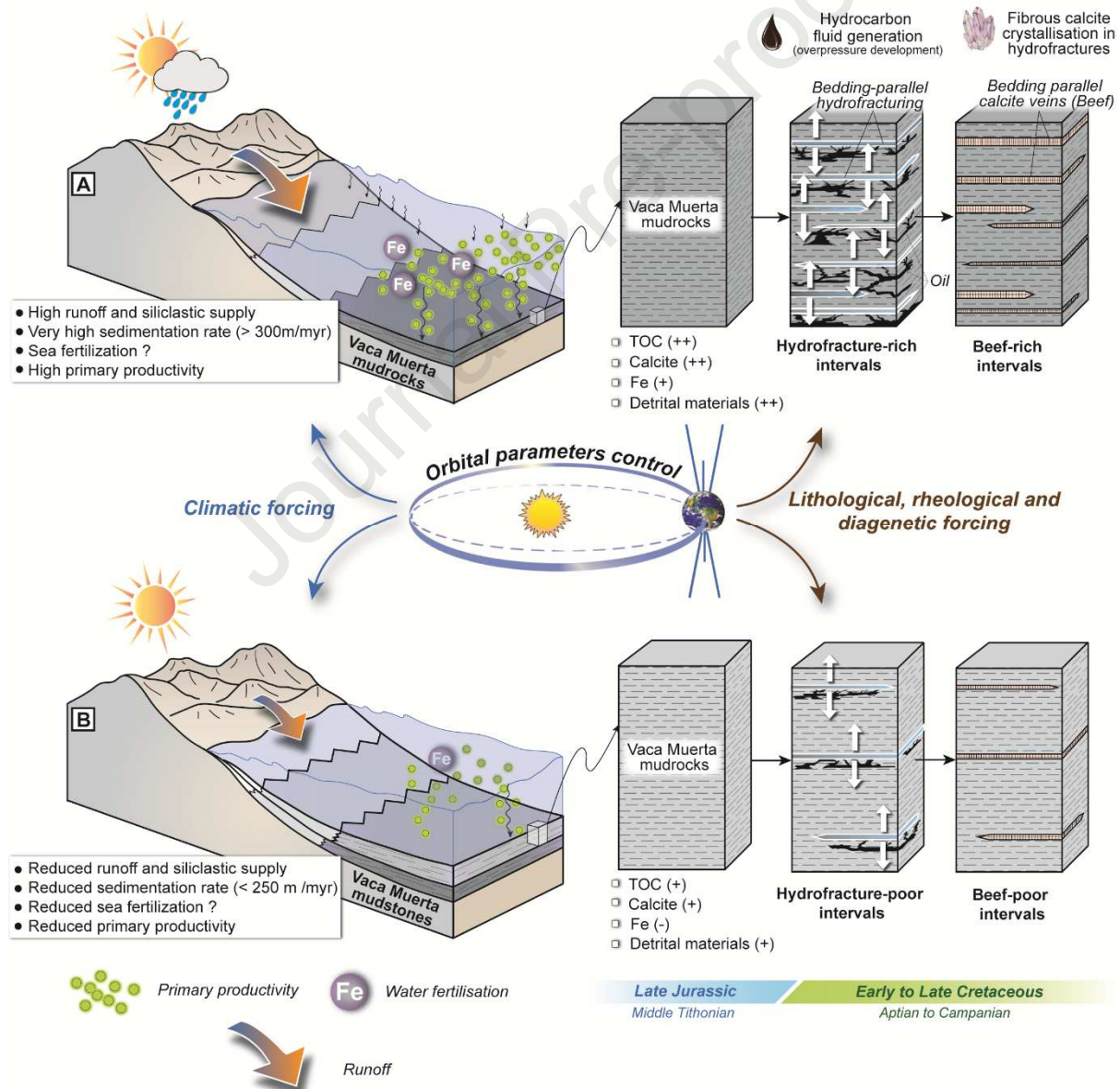
556 However, periods of increased sedimentary flux and siliciclastic supply, in relation with
557 enhanced runoff conditions during wetter climate are here supported by high ratios of
558 Quartz/Clay, Si/Al, Ti/Al, Ti/K and Fe/Al in the lower Huncal section that coincide with a
559 high sedimentation rate deduced from the thickness of the precession cycles ($\sim 300 \text{ m.myr}^{-1}$)
560 (Figs. 5 and 9A). Enhanced runoff and detrital export also correlate with an augmentation of
561 the TOC and iron content in the mudrocks (Fig. 5). Increased sedimentation rate and seawater
562 fertilization during wetter conditions can explain the positive feedback observed for the TOC
563 content in response to better organic matter preservation and increased primary productivity
564 (Arthur et al., 1987; Scasso et al., 2005; Armstrong et al., 2016). Classically in the Mesozoic,
565 organic-rich deposits become widespread at time of acceleration of the hydrolysing cycle
566 during more humid period (Dera et al., 2009; Föllmi, 2012; Martinez and Dera, 2015).

567 Otharan et al. (2020) also relate the high organic matter content in the Vaca Muerta mudrocks

568 to the basinward increase of detrital flux during humid periods through deposition of long-
569 lived muddy hyperpicnal flows triggered by extreme rivers discharges. Organic matter
570 incorporation during basinward transport and fast deposition could have enhanced organic
571 matter preservation and accumulation. In other locations of the basin, variations in TOC
572 content in the Vaca Muerta Fm have been related to palaeoproductivity during marine
573 transgression (highest TOC values) or dilution processes during marine regression (lowest
574 TOC values), combined with fluctuations of the redox conditions due to episodic restriction of
575 water-mass circulation (Kietzmann et al., 2016; Krim et al., 2017, 2019). The climatic-driven
576 model proposed here is not mutually exclusive with the role of eustatism evoked by
577 Kietzmann et al. (2016) in the coeval fluctuations in primary productivity, calcite export to
578 the sea bottom and the detrital input. Organic-rich mudrocks with an enhanced detrital
579 fraction are commonly encountered in transgressive phases in the Neuquén Basin (Kietzmann
580 et al., 2016) implying that orbitally-driven sea level fluctuations may have influenced the
581 lithological characteristics of the mudrocks and therefore the rheology and beef distribution of
582 the Vaca Muerta Fm. The very homogenous clayey lithology of the Vaca Muerta Fm
583 encountered in the Huncal area and the reduced window of observations and sampling (100
584 m-thick section) prevent the role of eustatism in controlling sedimentary cycles to be further
585 discussed.

586 At the Jurassic-Cretaceous boundary, a growing aridity evidenced by large evaporate deposits
587 coupled with clay mineralogical, palynological or numerical modelling data is worldwide
588 recorded (Hallam, 1982; Valdes et al., 1995; Price et al., 1997; Schnyder et al., 2006;
589 Sellwood and Valdes, 2008; Krim et al., 2017; Cameille et al., 2018; Turner & Huggett 2019).
590 Sedimentary intervals recording reduced sedimentation rate ($< 250 \text{ m.myr}^{-1}$) and lower values
591 of Quartz/Clay, Si/Al, Ti/Al, Ti/K and Fe/Al ratios may indicate periods of decrease in runoff
592 related to more arid climatic conditions (Fig. 9B). Reduced siliciclastic supply is also

593 combined to a decrease in mean TOC (from 2.4% to 1.7%). Fluctuations in runoff and
 594 sedimentary flux recorded in the Huncal area could also be related to latitudinal migration of
 595 the climatic belts as proposed by Sagasti (2005) and Krim et al. (2017) for the lower
 596 Cretaceous of the Neuquén Basin. Fluctuations in terrigenous supply to the basin occurred
 597 also likely in response to alternating climate regimes from arid to temperate depending on the
 598 configuration of the Earth's orbit (Sagasti, 2005). Similar conditions have also been suggested
 599 to occur during Late Jurassic times (Valdes et al., 1995, Armstrong et al., 2016).



600 **Figure 9.** Astroclimatic model for the Late Jurassic Vaca Muerta Fm in the Huncal area and its control on
 601 lithology and diagenesis. (A) Semi-arid conditions: higher runoff, siliclastic supply, TOC and sedimentation
 602

603 *rate. Organic-rich black shale facies favors the development of beef-rich intervals during diagenesis by*
604 *abundant hydrocarbon generation and subsequent hydrofracturing during the Cretaceous (Rodrigues et al.,*
605 *2009). (B) More arid conditions: Reduced runoff, siliclastic supply, TOC and sedimentation rate. The reduction*
606 *of organic content in black shales coincides with beef-poor intervals because of a decrease in hydrocarbon and*
607 *hydrofracture generation during diagenesis. Transitions between arid and semi-arid conditions are most*
608 *certainly related to latitudinal fluctuations of climatic belts in response to changes of the orbital parameters.*

609

610 Calcite content is surprisingly positively correlated with TOC values, sedimentation rate and
611 increased siliclastic supply. The opposite trend was observed in the Chos Malal area, north
612 of the Huncal area, with a negative correlation between TOC and calcite content (Kietzmann
613 et al., 2015; Rodriguez Banco et al., 2020). In this area, clear alternations between black
614 shales and limestone outcrop. The limestone beds there are interpreted as carbonate mud
615 produced in the platform and exported to the basin via density cascading currents (Rodriguez
616 Blanco et al., 2020). In the Huncal section, very few calciturbidite beds are intercalated within
617 a thick dark bituminous shale series. The increasing calcite content could correspond to the
618 enhanced preservation of calcareous bio-grains content in mudstones, in the conditions of a
619 TOC content predominantly influenced by palaeoproductivity. Alternatively, carbonate
620 authigenesis might explain the unpredictable correlation between TOC values, calcite content
621 and sedimentation rates. Authigenic calcium carbonate precipitation represents a non-
622 negligible component of the global carbon cycle that is thought to be enhanced where the
623 organic matter delivery to the sea floor is likely to be high (Sun and Turchyn, 2014). Miliken
624 et al. (2019) show evidence of radiolarian calcitization and demonstrate a correlation between
625 high TOC values and the precipitation of calcite during diagenesis of the Vaca Muerta
626 mudrocks north of the Huncal area. The localised presence of diffuse beef measuring less than
627 a millimetre, referred to as “microbeef” in Lejay et al. (2017) could have also been
628 incorporated into mudrock samples analysed in this study, possibly explaining the positive

629 correlation between TOC and calcite content. Although diagenesis might influence the calcite
630 content measured in shales from the Huncal section, Milliken et al. (2019) suggest that
631 characteristics of the diagenesis are primary controlled by the depositional setting, thus
632 explaining the relation between calcite content, TOC, sedimentation rates and Earth's orbital
633 parameters we establish in this study. We therefore propose that periodic fluctuations in
634 humidity/aridity have influenced sedimentary and biogenic processes that control any
635 lithological and rheological variations recorded in the black shales of the Huncal area (Fig. 9).
636 Paleoclimatic fluctuations have left an indelible fingerprint on the sedimentary record today
637 highlighted by the distribution of diagenetic features (e.g. beef) as demonstrated along the
638 Huncal section. This astroclimatic fingerprint on beef distribution could partially be
639 obliterated in some other sections of the Vaca Muerta Fm displaying beef-rich intervals,
640 especially where some relations between ash beds, fossils or calcitic concretions and beef
641 distribution have been evidenced (Rodrigues et al., 2009; Lejay et al., 2017; Weger et al.,
642 2019). Knowing that ash beds and concretions are very sparse in the studied section and that
643 lithology is rather homogeneous along the deciphered interval, most mechanical contrasts and
644 discontinuities used for hydrofracturing propagation derive from minor but recurrent changes
645 in sedimentary characteristics (detrital fraction, TOC) inherited from astroclimatic forcing we
646 demonstrated above. Based on these results, we suggest that the Milankovitch fingerprint on
647 beef distribution has certainly a best potential for preservation in basinal sections
648 characterized by high sedimentation rate, homogeneous lithology and low concentration of
649 mechanical contrasts inherited from aerial explosive volcanism and/or diagenesis.

650

651

652 **6. Conclusion**

653

654 We demonstrate that the Milankovitch cyclicity rule the processes controlling the composition
655 of organic-rich sediments in the basinal part of the Neuquén Basin. The relations and cycles
656 inferred from the statistical treatment of sedimentary (MS, elemental and mineralogical
657 ratios), biogenic (TOC) and diagenetic (beef distribution and thickness) signals revealed the
658 influence of the astroclimatic fingerprint recorded in sediments on processes controlling
659 mineralized fracture generation and distribution. During burial (probably once catagenesis
660 started), carbonate- and organic-rich sediments emplaced during enhanced wetter conditions
661 favoured the development of a dense bedding-parallel network of mineralised fractures along
662 weaker rheological plans. By slightly modifying the lithological and rheological
663 characteristics of the black shales deposited in the basin, reduced runoff and drier conditions
664 might have been the precursor explaining the occurrence of beef-poor intervals in the Huncal
665 section. Knowing the importance of mechanical discontinuities during hydraulic-fracture
666 stimulation, the astroclimatic memory recorded in the distribution of mineralized fracture
667 could help predicting the density of discontinuities in source rocks using a suitable mix of
668 mineralogical and geochemical proxies coupled to cyclostratigraphic signal analyses
669 following Milankovitch theory.

670

671

672 **Acknowledgement**

673

674 This study is part of the CYCLOBEEF project funded by “Institut National des Sciences de
675 L’Univers” through the programme Tellus and CESSUR (Connaissance et technologie du
676 Sous-Sol pour son exploitation et usage durable) action. The authors would like to thank
677 Salomé Larmier and Régis Mourgues for their contributions and discussions on the field
678 and Hector Leanza for his help in ammonoids determination. Matthieu Branellec is

679 thanked for the drawing of the beautiful geological map of the Neuquén Basin. We also
680 want to thank Jean-François Deconinck and François Baudin for their constructive
681 remarks during the elaboration of the project. Ludovic Bruneau is thanked for his
682 contribution in XRD and XRF measurements and Christelle Gruber is also thanked for
683 the production of thin sections.

684

685 **References**

686

687 Arthur, M.A., Zachos, J.C., Jones, D.S., 1987. Primary productivity and the Cretaceous/Tertiary
688 boundary event in the oceans. *Cretaceous Research* 8, 43–54. [https://doi.org/10.1016/0195-](https://doi.org/10.1016/0195-6671(87)90011-5)
689 [6671\(87\)90011-5](https://doi.org/10.1016/0195-6671(87)90011-5).

690 Aguirre-Urreta, B., Martinez, M., Schmitz, M., Lescano, M., Omarini, J., Tunik, M., Kuhnert, H.,
691 Concheuro, A., Rawson, P.F., Ramos, V.A., Reboulet, S., Noclin, N., Frederichs, T., Nickl,
692 A.L., Pälke, H., 2019. Interhemispheric radio-astrochronological calibration of the time scales
693 from the Andean and the Tethyan areas in the Valanginian–Hauterivian (Early
694 Cretaceous). *Gondwana Research* 104, 104–132. <https://doi.org/10.1016/j.gr.2019.01.006>.

695

696 Armstrong, H.A., Wagner, T., Herringshaw, L.G., Farnsworth, A.J., Lunt, D.J., Harland, M., Imber, J.,
697 Lopton, C., Atar, E.F., 2016. Hadley circulation and precipitation changes controlling black
698 shale deposition in the Late Jurassic Boreal Seaway. *Paleoceanography* 31, 1041–1053.
699 <https://doi.org/10.1002/2015PA002911>.

700

701 Carmeille, M., Bourillot, R., Brunet, M. F., Pellenard, P., Fürsich, F. T., Schnyder, J., Barrier, E.,
702 Blanpied, C., Sidorova, I., 2018. Architecture and sedimentary evolution of the southwestern
703 Gissar carbonate platform (Uzbekistan) during the Middle–Late Jurassic. *Marine and*
704 *Petroleum Geology* 97, 437–465. <https://doi.org/10.1016/j.marpetgeo.2018.07.021>.

705

- 706 Cobbold, P.R., Rodrigues, N., 2007. Seepage forces, important factors in the formation of horizontal
707 hydraulic fractures and bedding-parallel fibrous veins ('beef' and 'cone-in-
708 cone'). *Geofluids* 7, 313–322. <https://doi.org/10.1111/j.1468-8123.2007.00183.x>.
- 709 Cobbold, P.R., Zanella, A., Rodrigues, N., Løseth, H., 2013. Bedding-parallel fibrous veins (beef and
710 cone-in-cone): Worldwide occurrence and possible significance in terms of fluid overpressure,
711 hydrocarbon generation and mineralization. *Marine and Petroleum Geology* 43, 1–20.
712 <https://doi.org/10.1016/j.marpetgeo.2013.01.010>.
- 713 Cosgrove, J.W., 1995. The expression of hydraulic fracturing in rocks and sediments. *Geological*
714 *Society, London, Special Publications* 92, 187–196.
715 <https://doi.org/10.1144/GSL.SP.1995.092.01.10>.
- 716 Dera, G., Pellenard, P., Neige, P., Deconinck, J.F., Pucéat, E., Dommergues, J. L., 2009. Distribution
717 of clay minerals in Early Jurassic Peritethyan seas: palaeoclimatic significance inferred from
718 multiproxy comparisons. *Palaeogeography, Palaeoclimatology, Palaeoecology* 271, 39–51.
719 <https://doi.org/10.1016/j.palaeo.2008.09.010>.
- 720
- 721 Eberli, G.P., Weger, R.J., Tenaglia, M., Rueda, L., Rodriguez, L., Zeller, M., McNeil, D., Murray, S.,
722 Swart, P., 2017. The Unconventional Play in the Neuquén Basin, Argentina—Insights From the
723 Outcrop for the Subsurface, in: *Unconventional Resources Technology Conference*, Austin,
724 Texas, 24-26 July 2017 (pp. 2208-2219). Society of Exploration Geophysicists, American
725 Association of Petroleum Geologists, Society of Petroleum Engineers.
726 <https://doi.org/10.15530/URTEC-2017-2687581>.
- 727
- 728 Föllmi, K.B., 2012. Early Cretaceous life, climate and anoxia. *Cretaceous Research* 35, 230–257.
729 <https://doi.org/10.1016/j.cretres.2011.12.005>.
- 730
- 731 Franzese, J.R., Spalletti, L.A., 2001. Late Triassic-early Jurassic continental extension in southwestern
732 Gondwana: tectonic segmentation and pre-break-up rifting. *Journal of South American Earth*

- 733 Sciences 14, 257–270. [https://doi.org/10.1016/s0895-9811\(01\)00029-3](https://doi.org/10.1016/s0895-9811(01)00029-3).
- 734
- 735 Gale, J.F.W., Laubach, S.E., Olson, J.E., Eichhubl, P., Fall, A., 2014. Natural fractures in shale: A
736 review and new observations. AAPG Bulletin 98, 2165–2216.
737 <https://doi.org/10.1306/08121413151>.
- 738
- 739 Garrido, A.C., Parent, H., Brambilla, L., 2018. Tithonian stratigraphy and ammonite fauna of the
740 Vaca Muerta Formation in Mallín Quemado (Neuquén Basin, Argentina), with remarks on the
741 Andean chronostratigraphy. Volumina Jurassica 16, 1-26.
742 <https://doi.org/10.5604/01.3001.0012.0496>.
- 743
- 744
- 745 Grauls, D. 1999. Overpressures: Causal mechanisms, conventional and hydromechanical approaches.
746 Oil & Gas Science and Technology-Revue D IFP Energies Nouvelles 54, 667–678.
747 <https://doi.org/10.2516/ogst:1999056>.
- 748
- 749 Hallam, A., 1982. The Jurassic climate, in: Berger, W.H., Cromwell, J.C. (Eds.), Studies in
750 Geophysics: Climate in Earth History. National Academy Press, Washington, DC, 159–163.
- 751
- 752 Hallam A., 1994. Jurassic climates as inferred from the sedimentary and fossil record, in: Allen
753 J.R.L., Hoskins B.J., Sellwood B.W., Spicer R.A., Valdes P.J. (Eds.), Palaeoclimates and
754 their Modelling. Springer, Dordrecht, 79–88. [https://doi.org/10.1007/978-94-011-1254-](https://doi.org/10.1007/978-94-011-1254-3_10)
755 [3_10](https://doi.org/10.1007/978-94-011-1254-3_10).
- 756
- 757 Hinnov, L.A., 2018. Cyclostratigraphy and Astrochronology in 2018, in: Montenari, M. (Ed.),
758 Stratigraphy and Timescales vol. 3: Cyclostratigraphy and Astrochronology, 1–80.
759 <https://doi.org/10.1016/bs.sats.2018.08.004>.

760

761 Hinnov, L.A., Schulz, M., Yiou, P., 2002. Interhemispheric space-time attributes of the Dansgaard-
762 Oeschger oscillations between 0-100 ka. *Quaternary Science Reviews* 21, 1213–1228.
763 [https://doi.org/10.1016/S0277-3791\(01\)00140-8](https://doi.org/10.1016/S0277-3791(01)00140-8).

764

765 Howell, J.A., Schwarz, E., Spalletti, L.A., Veiga, G.D., 2005. The Neuquen Basin: an overview, in:
766 Veiga, G.D., Spalletti, L.A., Howell, J.A., Schwarz, E. (Eds.), *The Neuquén Basin, Argentina:
767 A Case Study in Sequence Stratigraphy and Basin Dynamics*, Geological Society, London,
768 *Special Publications* 252, 1–14. <https://doi.org/10.1144/gsl.sp.2005.252.01.01>.

769

770 Hunt, C.P., Moskovitz, B.M., Banerjee, S.K., 1995. Magnetic Properties of Rocks and Minerals, in:
771 Ahrens, T.J. (Ed.), *Rock Physics and Phase Relations: A Handbook of Physical Constants*.
772 *AGU Reference Shelf* 3, American Geophysical Union, Washington DC, 189–204.
773 <https://doi.org/10.1029/RF003p0189>.

774

775 Kietzmann, D.A., Palma, R.M., Riccardi, A.C., Martín-Chivelet, J., López-Gómez, J., 2014.
776 *Sedimentology and sequence stratigraphy of a Tithonian-Valanginian carbonate ramp (Vaca
777 Muerta Formation): A misunderstood exceptional source rock in the Southern Mendoza area
778 of the Neuquen Basin, Argentina. *Sedimentary Geology* 302, 64–86.*
779 <https://doi.org/10.1016/j.sedgeo.2014.01.002>.

780

781 Kietzmann, D.A., Palma, R.M., Iglesia Llanos, M.P., 2015. Cyclostratigraphy of an orbitally-driven
782 Tithonian-Valanginian carbonate ramp succession, Southern Mendoza, Argentina:
783 Implications for the Jurassic-Cretaceous boundary in the Neuquen Basin. *Sedimentary
784 Geology* 315, 29–46. <https://doi.org/10.1016/j.sedgeo.2014.10.002>.

785

786 Kietzmann, D.A., Ambrosio, A.L., Suriano, J., Alonso, M.S., Tomassini, F.G., Depine, G., Repol, D.,

- 787 2016. The Vaca Muerta–Quintuco system (Tithonian–Valanginian) in the Neuquén Basin,
788 Argentina: A view from the outcrops in the Chos Malal fold and thrust belt. AAPG Bulletin
789 100, 743–771. <https://doi.org/10.1306/02101615121>.
- 790
- 791 Kietzmann, D.A., Iglesia Llanos, M.P., Kohan Martínez, M., 2018. Astronomical Calibration of the
792 Tithonian–Berriasian in the Neuquén Basin, Argentina: A Contribution From the Southern
793 Hemisphere to the Geologic Time Scale, in: Montenari, M. (Ed.), Stratigraphy and Timescales
794 3, Cyclostratigraphy and Atrochronology, 327–355.
795 <https://doi.org/10.1016/bs.sats.2018.07.003>.
- 796
- 797 Kohan Martínez, M., Kietzmann, D.A., Iglesia Llanos, M.P., Leanza, H.A., Luppo, T. 2018.
798 Magnetostratigraphy and cyclostratigraphy of the Tithonian interval from the Vaca Muerta
799 Formation, southern Neuquen Basin, Argentina. Journal of South American Earth Sciences
800 85, 209–228. <https://doi.org/10.1016/j.jsames.2018.05.010>.
- 801
- 802 Krim, N., Bonnel, C., Tribovillard, N., Imbert, P., Aubourg, C., Riboulleau, A., Bout-Roumazeilles,
803 V., Hoareau, G., Fasentieux, B., 2017. Palaeoenvironmental evolution of the southern Neuquén
804 basin (Argentina) during the Tithonian-Berriasian (Vaca Muerta and Picun Leufu Formations):
805 a multi-proxy approach. BSGF - Earth Sciences Bulletin 188, 34.
806 <https://doi.org/10.1051/bsgf/2017196>.
- 807
- 808 Krim, N., Tribovillard, N., Riboulleau, A., Bout-Roumazeilles, V., Bonnel, C., Imbert, P., Aubourg,
809 C., Hoareau, G., Fasentieux, B., 2019. Reconstruction of palaeoenvironmental conditions of
810 the Vaca Muerta formation in the southern part of the Neuquén Basin (Tithonian-
811 Valanginian): Evidences of initial short-lived development of anoxia. Marine and Petroleum
812 Geology 103, 176-201. <https://doi.org/10.1016/j.marpetgeo.2019.02.011>.
- 813
- 814 Larmier, S., 2020. Génération de fluides, migration et fracturation au sein des roches mères : cas de

- 815 la formation de Vaca Muerta, bassin de Neuquén, Argentine (PhD Thesis) Le Mans
816 Université, Le Mans (507 pp.).
817
- 818 Laskar, J., Fienga, A., Gastineau, M., Manche, H., 2011. La2010: a new orbital solution for the long-
819 term motion of the Earth. *Astronomy and Astrophysics* 532, A89. [https://doi.org/](https://doi.org/10.1051/0004-6361/201116836)
820 [10.1051/0004-6361/201116836](https://doi.org/10.1051/0004-6361/201116836).
- 821
- 822 Leanza, H.A., Hugo, C.A., Repol, D., Salvarredy Aranguren, M., 2003. The Huncal Member (Lower
823 Berriasian): a turbidite episode in the Vaca Muerte Formation, Neuquén basin, Argentina.
824 Miembro Huncal (Berriasiano inferior): un episodio turbidítico en la Formación Vaca Muerta,
825 Cuenca Neuquina, Argentina. *Revista de la Asociación Geológica Argentina* 58, 248–254.
826
- 827 Leanza, H.A., Sattler, F., Martínez, R., Carbone, O., 2011. La Formación Vaca Muerta y Equivalentes
828 (Jurásico Tardío–Cretácico Temprano) en la Cuenca Neuquina. *Geología y Recursos*
829 *Naturales de la Provincia del Neuquén, Neuquén*. Buenos Aires. *Revista de la Asociación*
830 *Geológica Argentina*, 113–129.
831
- 832 Legarreta, L., Gulisano, C.A., 1989. Análisis estratigráfico secuencial de la Cuenca Neuquina
833 (Triásico superior-Terciario inferior, Argentina), in: Chebli, G., Spalletti, L.A. (Eds.), *Serie*
834 *Correlación Geológica 6, Cuencas Sedimentarias Argentina*, Universidad Nacional de
835 Tucumán, Tucumán, 221–243.
836
- 837 Legarreta, L., Uliana, M.A., 1991. Jurassic—Marine Oscillations and Geometry of Back-Arc Basin
838 Fill, Central Argentine Andes, in: Macdonald, D.I.M (Ed.), *Sedimentation, Tectonics and*
839 *Eustasy: Sea-Level Changes at Active Margins*, Special Publication of the International
840 Association of Sedimentologists 12, Blackwell Scientific Publications, Oxford, 429-450.
841 <https://doi.org/10.1002/9781444303896.ch23>.

842

843 Lejay, A., Larmier, S., Rutman, P., & Gelin, F., 2017. The Role of Porosity in the Development of
844 Parallel Bedded Calcite Filled Fractures (or Beef) in the Vaca Muerta: An Integrated Analysis
845 From High Resolution Core Data. In *Unconventional Resources Technology Conference*,
846 *Austin, Texas, 24-26 July 2017* (pp. 394-409). Society of Exploration Geophysicists, American
847 Association of Petroleum Geologists, Society of Petroleum Engineers.

848

849 Martinez, M., Dera, G., 2015. Orbital pacing of carbon fluxes by a ~9-My eccentricity cycle during
850 the Mesozoic. *Proceedings of the National Academy of Sciences* 112, 12604–12609.
851 <https://doi.org/10.1073/pnas.1419946112>.

852

853 Meng, Q., Hooker, J., Cartwright, J., 2017. Early overpressuring in organic-rich shales during burial:
854 evidence from fibrous calcite veins in the Lower Jurassic Shales-with-Beef Member in the
855 Wessex Basin, UK. *Journal of the Geological Society* 174, 869–882.
856 <https://doi.org/10.1144/jgs2016-146>.

857

858 Meng, Q., Hooker, J., Cartwright, J., 2018. Role of pressure solution in the formation of bedding-
859 parallel calcite veins in an immature shale (Cretaceous, southern UK). *Geological Magazine* 156, 918–
860 934. <https://doi.org/10.1017/S0016756818000377>.

861

862 Meyers, S. R., 2014. *Astrochron: An R Package for Astrochronology (Version 0.3)*

863

864 Milankovitch, M., 1920. *Théorie mathématique des phénomènes thermiques produits par la radiation*
865 *solaire*. Gauthier-Villars, Paris.

866

867 Milliken, K.L., Reed, R. M., McCarty, D. K., Bishop, J., Lipinski, C.J., Fischer, T.B., Crousse, L.,
868 Reijenstein, H., 2019. Grain assemblages and diagenesis in the Vaca Muerta Formation (Jurassic-

- 869 Cretaceous), Neuquén Basin, Argentina. *Sedimentary Geology* 380, 45–64.
870 <https://doi.org/10.1016/j.sedgeo.2018.11.007>.
- 871
- 872 Moore, D.M., Reynolds, R.C., 1997. X-Ray Diffraction and the Identification and Analysis of Clay
873 Minerals, 2nd edition. Oxford University Press, Inc., New York.
- 874
- 875 Otharán, G.A., Zavala, C., Arcuri, M., Di Meglio, M., Zorzano, A., Marchal, D., Köhler, G., 2020.
876 Facies analysis of organic-rich fluid mud flow deposits. The lower section of the Vaca Muerta
877 Formation (Tithonian) at basinal positions, Neuquén Basin, Argentina. *Andean Geology* 47,
878 384-417. <http://dx.doi.org/10.5027/andgeoV47n2-3061>.
- 879
- 880 Pellenard P., Deconinck J.-F., 2006. Mineralogical variability of Callovo-Oxfordian clays from the
881 Paris Basin and the Subalpine Basin. *Comptes Rendus Geoscience* 338, 854–866.
882 <https://doi.org/10.1016/j.crte.2006.05.008>.
- 883
- 884 Pellenard, P., Tramoy, R., Pucéat, E., Huret, E., Martinez, M., Bruneau, L., Thierry, J., 2014. Carbon
885 cycle and sea-water palaeotemperature evolution at the Middle–Late Jurassic transition,
886 eastern Paris Basin (France). *Marine and Petroleum Geology* 53, 30–43.
887 <https://doi.org/10.1016/j.marpetgeo.2013.07.002>.
- 888
- 889 Petschick, R., 2001. MacDiff: the user-friendly x-ray powder diffractometry analysis tool for
890 Macintosh computers.
- 891
- 892 Parent H., Garrido A.C., Scherzinger A., Schweigert G., Fözy I., 2015. The Tithonian-Lower
893 Valanginian stratigraphy and ammonite fauna of the Vaca Muerta Formation in Pampa Tril,
894 Neuquén Basin, Argentina. *Boletín del Instituto de Fisiografía y Geología* 86, 1–96.
- 895

- 896 Price, G.D., Valdes, P.J., Sellwood, B. W., 1997. Quantitative palaeoclimate GCM validation: Late
897 Jurassic and mid-Cretaceous case studies. *Journal of the Geological Society* 154, 769–772.
898 <https://doi.org/10.1144/gsjgs.154.5.0769>.
899
- 900 Ramos, V. A., Naipauer, M., Leanza, H. A., & Sigismondi, M. E., 2019. The Vaca Muerta Formation
901 of the Neuquén Basin: An Exceptional Setting along the Andean Continental Margin. *AAPG Memoir*
902 120 Vaca Muerta Fm.
903
- 904 Riccardi, A., 2015. Remarks on the Tithonian-Berriasian ammonite biostratigraphy of west central
905 Argentina. *Volumina Jurassica* 13, 23–52.
906
- 907 Rodrigues, N., Cobbold, P.R., Loseth, H., Ruffet, G., 2009. Widespread bedding-parallel veins of
908 fibrous calcite ('beef') in a mature source rock (Vaca Muerta Fm, Neuquén Basin, Argentina):
909 evidence for overpressure and horizontal compression. *Journal of the Geological Society* 166,
910 695–709. doi.org/10.1144/0016-76492008-111.
911
- 912 Rodriguez Blanco, L., Eberli, G.P., Weger, R.J., Swart, P.K., Tenaglia, M., Rueda Sanchez, L.E.,
913 McNeill, and D.F., 2020. Periplatform ooze in a mixed siliciclastic-carbonate system - Vaca
914 Muerta Formation, Argentina. *Sedimentary Geology* 396, 105521.
- 915 Sagasti, G., 2005. Hemipelagic record of orbitally-induced dilution cycles in Lower Cretaceous
916 sediments of the Neuquén Basin. *Geological Society, London, Special Publications* 252, 231–
917 250. <https://doi.org/10.1144/GSL.SP.2005.252.01.11>.
- 918 Scasso, R.A., Alonso, M.S., Lanés, S., Villar, H.J., Laffitte, G., 2005. Geochemistry and petrology of a
919 Middle Tithonian limestone-marl rhythmite in the Neuquén Basin, Argentina: depositional and
920 burial history. *Geological Society, London, Special Publications* 252, 207–229.
921 <https://doi.org/10.1144/GSL.SP.2005.252.01.10>.

- 922 Schnyder, J., Ruffell, A., Deconinck, J.-F., Baudin, F., 2006. Conjunctive use of spectral gamma-ray
923 logs and clay mineralogy in defining late Jurassic–early Cretaceous palaeoclimate change
924 (Dorset, UK). *Palaeogeography, Palaeoclimatology, Palaeoecology*, 229, 303–320.
925 <https://doi.org/10.1016/j.palaeo.2005.06.027>.
- 926 Sellwood, B.W., Valdes P.J., 2008. Jurassic climates. *Proceedings of the Geologists Association* 119,
927 5–17. [https://doi.org/10.1016/s0016-7878\(59\)80068-7](https://doi.org/10.1016/s0016-7878(59)80068-7).
- 928
- 929 Spalletti, L.A., Franzese, J.R., Matheos, S.D., Schwarz, E., 2000. Sequence stratigraphy of a tidally
930 dominated carbonate-siliciclastic ramp; the Tithonian-Early Berriasian of the Southern
931 Neuquén Basin, Argentina. *Journal of the Geological Society* 157, 433–446.
932 <https://doi.org/10.1144/jgs.157.2.433>.
- 933
- 934 Strasser, A., Hilgen, F.J., Heckel, P.H., 2006. Cyclostratigraphy – concepts, definitions, and
935 applications. *Newsletters on Stratigraphy* 42, 75–114. [https://doi.org/10.1127/0078-](https://doi.org/10.1127/0078-0421/2006/0042-0075)
936 [0421/2006/0042-0075](https://doi.org/10.1127/0078-0421/2006/0042-0075).
- 937
- 938 Sucha, V., Kraus, I., Gerthofferova, H., Petes, J., Serekova, M., 1993. Smectite to illite conversion in
939 bentonites and shales of the East Slovak Basin. *Clay Minerals* 28, 243–243.
940 <https://doi.org/10.1180/claymin.1993.028.2.06>.
- 941
- 942 Sun, X., Turchyn, A.V., 2014. Significant contribution of authigenic carbonate to marine carbon
943 burial. *Nature Geoscience* 7, 201–204. <https://doi.org/10.1038/ngeo2070>.
- 944
- 945 Swarbrick, R.E., Osborne, M.J., 1998. Mechanisms that generate abnormal pressures: an overview, in:
946 Law B.E., Ulmishek G.F., Slavin V.I. (Eds.), *Abnormal pressures in hydrocarbon*
947 *environments*. *American Association of Petroleum Geologists Memoir* 70, 13–34.
- 948

949

950 Thomson, D.J., 1982. Spectrum Estimation and Harmonic-Analysis. Proceedings of the IEEE 70,
951 1055–1096. <https://doi.org/10.1109/PROC.1982.12433>.

952

953 Thomson, D.J., 1990. Quadratic-Inverse Spectrum Estimates: Applications to Paleoclimatology.
954 Philosophical Transactions of the Royal Society of London Series a-Mathematical Physical
955 and Engineering Sciences 332, 539–597. <https://doi.org/10.1098/rsta.1990.0130>.

956

957 Turner, H.E., Huggett, J.M., 2019. Late Jurassic–Early Cretaceous climate change record in clay
958 minerals of the Norwegian-Greenland Seaway. *Palaeogeography, Palaeoclimatology,*
959 *Palaeoecology*, 534, 109331. <https://doi.org/10.1016/j.palaeo.2019.109331>.

960

961 Ukar, E., Lopez, R.G., Laubach, S.E., Gale, J.F.W., Manceda, R., Marrett, R., 2017. Microfractures in
962 bed-parallel veins (beef) as predictors of vertical macrofractures in shale: Vaca Muerta
963 Formation, Agrio Fold-and-Thrust Belt, Argentina. *Journal of South American Earth Sciences*
964 79, 152–169. <https://doi.org/10.1016/j.jsames.2017.07.015>.

965

966 Valdes, P.J., Sellwood, B.W., Price, G.D., 1995. Modelling Late Jurassic Milankovitch climate
967 variations, in: House, M.R., Gale, A.S. (Eds.), *Orbital Forcing Timescales and*
968 *Cyclostratigraphy*, Geological Society, London, Special Publications 85, pp. 115–
969 132. <https://doi.org/10.1144/GSL.SP.1995.085.01.07>.

970

971 Vennari, V.V., 2016. Tithonian ammonoids (cephalopoda, Ammonoidea) from the Vaca Muerta
972 Formation, Neuquén basin, west-central Argentina. *Palaeontographica Abteilung A*, 85 –165.
973 <https://doi.org/10.1127/pala/306/2016/85>.

974

975 Vergani, G.D., Tankard, A.J., Belotti, H.J., Welsink, H.J., 1995. Tectonic evolution and
976 paleogeography of the Neuquén Basin, Argentina, in: Tankard, A.J., Suarez Soruco, R.

- 977 Welsink, H.J. (Eds.), *Petroleum Basins of South America*, AAPG Memoirs 62, 383–402.
978 <https://doi.org/10.1306/M62593C19>.
979
- 980 Waltham, D., 2015. Milankovitch period uncertainties and their impact on cyclostratigraphy. *Journal*
981 *of Sedimentary Research* 85, 990–998. <https://doi.org/10.2110/jsr.2015.66>.
982
- 983 Weedon, G.P., 2003. *Time-Series Analysis and Cyclostratigraphy*, Cambridge University Press,
984 Cambridge.
985
- 986 Weger, R.J., Murray, S.T., McNeill, D.F., Swart, P.K., Eberli, G.P., Blanco, L.R., Rueda, L., 2019.
987 Paleo thermometry and distribution of calcite beef in the Vaca Muerta Formation, Neuquén
988 Basin, Argentina. *AAPG Bulletin* 103, 931–950. <https://doi.org/10.1306/10021817384>.
989
- 990 Zanella, A., Cobbold, P.R., Boassen, T., 2015a. Natural hydraulic fractures in the Wessex Basin, SW
991 England: Widespread distribution, composition and history. *Marine and Petroleum*
992 *Geology* 68, 438–448. <https://doi.org/10.1016/j.marpetgeo.2015.09.005>.
993
- 994 Zanella, A., Cobbold, P. R., Ruffet, G., & Leanza, H. A., 2015b. Geological evidence for fluid
995 overpressure, hydraulic fracturing and strong heating during maturation and migration of
996 hydrocarbons in Mesozoic rocks of the northern Neuquén Basin, Mendoza Province,
997 Argentina. *Journal of South American Earth Sciences* 62, 229–242.
998 <https://doi.org/10.1016/j.jsames.2015.06.006>.
999
- 1000 Zanella, A., Cobbold, P. R., Rodrigues, N., Loseth, H., Jolivet; M., Gouttefangeas, F., Chew, D., 2020.
1001 Source rocks in foreland basins: a preferential context for the development of natural hydraulic
1002 fractures. *AAPG Bulletin*.
1003

1004

1005 Zeiss, A., Leanza, H.A., 2010. Upper Jurassic (Tithonian) ammonites from the lithographic limestones
1006 of the Zapala region, Neuquén Basin, Argentina. *Beringeria* 41, 25–75.

1007

1008 Zhang, J., Jiang, Z., Jiang, X., Wang, S., Liang, C., & Wu, M., 2016. "Oil generation induces sparry
1009 calcite formation in lacustrine mudrock, Eocene of east China. *Marine and Petroleum Geology*
1010 71, 344–359. <https://doi.org/10.1016/j.marpetgeo.2016.01.007>.

1011

Journal Pre-proof

Highlights

- Times-series analyses on sedimentary proxies and diagenetic calcite veins (beef)
- Milankovitch cycles controlled detrital input and preservation of organic matter
- Imprint of the Milankovitch cycles on the recurrence and thickness of beef
- Initial climate forcing induces differential diagenesis and control beef distribution in source rocks

Journal Pre-proof

Declaration of interests

The authors declare that they have no known competing financial interests or personal relationships that could have appeared to influence the work reported in this paper.

The authors declare the following financial interests/personal relationships which may be considered as potential competing interests:

Journal Pre-proof